nature energy

Article

https://doi.org/10.1038/s41560-026-02027-4

Contact-triggered molecular interactions enable structural refinement of perovskite layers in solar cells

Received: 22 May 2025

Accepted: 3 March 2026

Published online: 25 March 2026

Check for updates

Seungmin Lee[1,2,13], Yeoun-Woo Jang[3,4,5,13], Hyeonah Cho[1], Jihoo Lim[6], Jiahao Xie[2], Hyojin Hong[1], Woocheol Han[1], Oui Jin Oh[1], Dong Hyun Kim[1], Dong Hun Kang[1], Wonjin Cho[3], Hyun Jung Mun[7], Tae Joo Shin[8], Jae Sung Yun[9,10], Josh Davies-Jones[11], Philip R. Davies[11], Yanfa Yan[2], Mansoo Choi[3,4] & Jun Hong Noh[1,12]

Molecular interactions are crucial to improving the efficiency and stability of perovskite solar cells, yet current solution-based approaches relying on molecular incorporation or surface passivation show inherent limitations in separately controlling these interactions. Here we reveal an intrinsic interfacial interaction that arises from simple contact between individually crystallized two-dimensional and three-dimensional perovskites without mixing or permanent bonding. We define this contact-triggered cationic interaction (CCI), which reversibly constrains molecular degrees of freedom, suppresses phase transitions, enhances carrier lifetimes and induces a unique recrystallization of the three-dimensional framework. This CCI-driven recrystallization produces refined $FAPbI_3$ with improved cation homogeneity, reduced lattice disorder and superior optoelectronic properties. Devices using CCI-driven $FAPbI_3$ achieve 26.25% efficiency (25.61% certified) and retain a projected operational lifetime exceeding 20,000 h. Our findings provide the first quantitative evidence that intrinsic interfacial cationic interactions can directly influence perovskite material quality and device performance.

Molecular interactions in the ABX_3 crystal structure of three-dimensional (3D) perovskites, including those involving additives or passivating molecules, critically govern perovskite solar cells (PSCs) performance, alongside composition[1,2], microstructure[3,4] and crystallinity[5,6]. These interactions determine the stability[7], optoelectronic properties[8] and charge transport[9]. From a crystallographic perspective, bulky organic spacer cations, which are chemically stable linked by van der Waals interactions, have further enabled dimensional control from 3D to two-dimensional (2D) perovskite crystal structures through intermolecular interaction[10,11].

In PSC research, molecular interactions are primarily investigated through solution-based processes. Additives such as dimethyl sulfoxide and *n*-methyl-2-pyrrolidinone enhance film quality[12,13], by interacting with precursors and forming intermediate adducts yielding high-quality films[5,14,15] and improved stability[16]. Bulky organic spacers are also incorporated either directly into precursor solutions[17,18] or applied separately at interfaces[19–21] to form 2D perovskite, regulate crystallization, enhance stability and improve device performance.

Despite the ease of processing and the impressive device performance achieved through these solution-based molecular interactions, it is crucial to recognize their inherent limitations. Indeed, such solution-based approaches intrinsically limit independent control over molecular interactions, these processes inherently involve permanent bonding, cation exchange and interdiffusion[22,23]. In addition, they

A full list of affiliations appears at the end of the paper. e-mail: junhnoh@korea.ac.kr

are highly sensitive to humidity[24] and temperature[25], often causing pinholes[26] and residual solvents[27] and nanoscale impurities[28]. Device environments involve multiple simultaneous interactions, including mixed compositions and dimensional heterojunctions, which further complicate the isolation of individual effects. This complexity obscures the identification of distinct interaction mechanisms and hinders a mechanistic understanding of performance loss and long-term instability in PSCs.

By contrast, solvent-free solid-state reaction techniques offer an efficient platform for selectively investigating molecular interactions[29,30]. Owing to the soft crystalline nature of perovskites, these materials are highly responsive to external stimuli[31], enabling additional growth and bulk reformation through solid-state reactions. Although such processes were initially explored at the microscale[32,33], recent extension to the nanoscale has broadened the scope of solid-state interaction studies[34,35]. Specifically, solid-state interactions between 2D and 3D perovskites provide a driving force for the growth of 2D layers on 3D perovskite surfaces, yielding crystallinity superior to that achieved by solution processing[30]. These 2D layers further impart multifunctional properties, including defect passivation, localized electric fields generation[29] and ferroelectric properties[36] thereby drawing increasing attention to solid-state heterodimensional interactions[37–39]. With respect to the control of molecular interactions, the solid-state reaction between 2D and 3D perovskites, particularly when employing 2D perovskite solid films, holds promising potential as a unique platform for precise and tuneable molecular interactions. Unlike the limited selection of A-site molecules in 3D perovskites, the broader range of organic spacers available in 2D perovskites enables more diverse and controllable molecular interactions[40,41].

Here, we introduce contact-triggered cationic interaction (CCI), a previously unrecognized phenomenon in which simple physical contact between individually crystallized 2D and 3D perovskite framework-embedded molecules induces pronounced and reversible changes in material properties, without permanent bonding, chemical reaction or junction formation. At these well-defined interfaces, bulky spacer chains in the 2D perovskite deform and engage in dipole-induced dipole interactions with formamidinium (FA) cations in the 3D perovskite. Increasing alkyl-chain length strengthens these interactions by increasing available contact sites, progressively constraining molecular degrees of freedom. Remarkably, CCI alone suppresses phase transitions, extends carrier lifetimes and triggers unique recrystallization of the 3D perovskite lattice into a stable tetragonal phase through subsequent heating, all without any incorporating 2D components or forming permanent bilayer. The CCI-driven $FAPbI_3$ exhibits markedly improved cation homogeneity, crystal orientation and optoelectronic properties. Solar cells based on this material achieve a power conversion efficiency (PCE) of 26.25% (certified at 25.61%), retains 95.2% of initial efficiency after 2,000 h of operation and exhibit a projected lifetime ~24,800 h. This study provides the quantitative and experimental evidence that intrinsic interfacial cationic interactions decisively govern material properties, device performance and long-term stability, offering a rational framework for molecular-level interface design in halide perovskite.

CCI

Designing or leveraging perovskite interfaces demands a deep understanding of interfacial interactions, including quantifying their strengths and assessing the resulting micro- and macroscopic changes. To isolate interface-driven phenomena, the interfacial structure must be well defined, and permanent chemical reactions or direct bonding should be avoided. Accordingly, we fabricate framework-structured perovskite thin films independently and analysed the interactions arising solely from simple surface contact (Fig. 1a). This contact-based configuration prevents chemical reactions or permanent junction formation at the interface and enables reversible recovery upon contact removal. We term this non-permanent interaction CCI, which can be reversibly activated and deactivated through the contact and separation.

In framework-structured perovskites, cations occupy the sites between Pb–I octahedra. At the surface, bulky cation amine groups orient inward in 2D perovskites, more prominently than in 3D perovskites with freely rotating cage cations. This structural regularity enables well-defined surface interactions even under simple contact conditions. We selected alkyl amine-based 2D perovskites and FA-based 3D perovskites as interface components and systematically varied only in alkyl-chain length: C4N1 (butylammonium lead iodide, $(BA)_2PbI_4$), C8N1 (octylammonium lead iodide, $(OA)_2PbI_4$) and C12N1 (dodecylammonium lead iodide, $(DDA)_2PbI_4$).

To verify interfacial effects on photoexcited charge behaviour, we performed in situ steady-state photoluminescence (PL) measurements. Figure 1b shows the in situ PL map and integrated PL intensity obtained by sequentially placing and removing 2D perovskites on the same 3D film. The PL signal near 800 nm increases sequentially from C4N1 to C8N1 to C12N1 and fully reverts to its initial state upon removal of the 2D perovskite layer. This signal 'node,' observed using the same 3D perovskite film, indicates that simple contact under ambient conditions does not induce chemical reactions or permanent junctions. In situ photoconductivity measurements further corroborate this attribution to the CCI (Supplementary Fig. 1), confirming that the observed changes arise from CCI and depend on cation type (Supplementary Note 1).

The constructed 2D/3D interface includes Pb–I octahedra, FA cations and framework-embedded bulky cations, with possible interactions such as dipole–dipole, dipole-induced dipole, hydrogen bonding and van der Waals forces. To identify interacting components, interaction strength and resulting changes, we employed density functional theory (DFT) simulations. Figure 2a illustrates the interface configuration under simple contact for each alkyl-chain length. Upon contact, bulky cations bend at the interface with deformation increasing with chain length (Supplementary Fig. 2). Differential charge density analysis reveals polarization within the 2D perovskite chains and indicates that the interactions are dominated not by amine hydrogen bonding but by long alkyl chains interacting with 3D octahedra and cage cations. Major contributions arise from specific components, including terminal regions of the 3D perovskite, segments of the octahedra, the FA cation and terminal regions of the 2D chains. Longer alkyl chains increase both the number of interaction sites and the overall interaction strength. The interaction strength was quantified via adsorption energy (E_{ads}), which increased in magnitude with alkyl-chain length from −198 meV to −592 meV (Fig. 2b). This metric enables comparisons of interaction strengths across contact scenarios. Standardizing the interaction strength provides a basis for designing interfaces based on interaction mechanisms that are applicable to various perovskite systems with modified cations (for example, FA replaced by MA, Cs or alkyl/aryl cations), central metals (Pb replaced by Sn) or halides (Cl, Br and I combinations). Despite involving nonpolar alkyl chains, these adsorption energies are relatively strong due to dipole-induced dipole interactions with FA cations. As shown in Fig. 2c, strong interaction increases the FA rotational activation barrier along both the C–H and N–N axes, notably from 0.79 eV to 1.12 eV along the C–N axis (Supplementary Fig. 3). Aligned dipoles under CCI generate localized fields that can influence carrier dynamics during exciton separation[42,43]. Further technical details regarding the simulation and energetic analysis are provided in Supplementary Note 2.

Figure 2d presents the PL decay results as a function of the 2D material used to activate the CCI. The carrier lifetime increases further under CCI conditions with materials exhibiting stronger interaction strength. Improvements are observed both at the surface and in the bulk but primarily at the surface (Supplementary Fig. 4 and Supplementary Table 1). Notably, the extent of surface improvement

https://doi.org/10.1038/s41560-026-02027-4

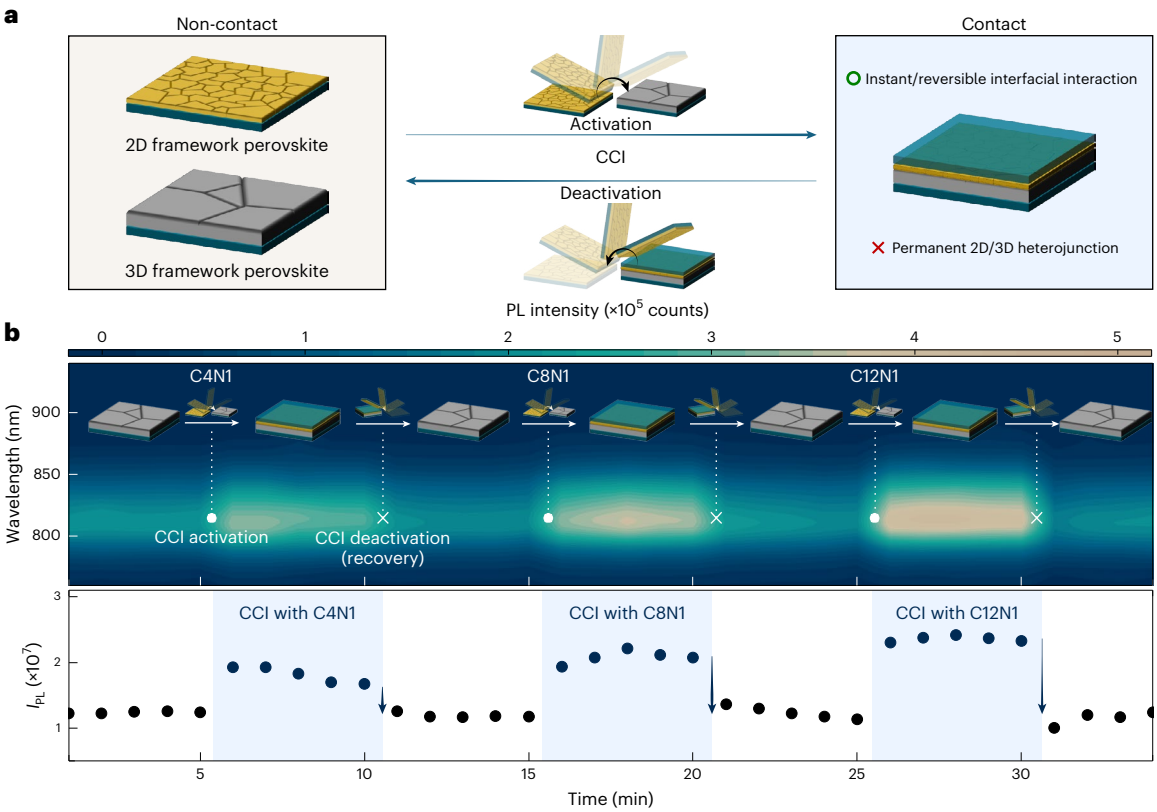

Fig. 1 | CCI. a, A schematic of CCI between framework-embedded molecules of 3D and 2D perovskites. Deactivation (contact removal) reversibly restores the system to its initial 3D perovskite state. **b**, In situ PL map and integrated PL intensity (I_{PL}) of 3D $FAPbI_3$ during repeated CCI activation–deactivation cycles with 2D framework-embedded bulky spacers on the same 3D film. The inset schematics illustrate the in situ experimental sequence using different spacer molecules (C4N1, C8N1 and C12N1). These cycles were repeated at fixed intervals, showing immediate PL enhancement upon activation and instant PL quenching upon inactivation over multiple cycles.

aligns closely with the trend in interaction strength. Experiments involving contact with non-framework cation salt layers demonstrate that without surface regularity, the effects of interactions are less pronounced (Extended Data Fig. 1). Compared with the trends or values observed in conventional passivation or permanent junction formation, the lifetime enhancement trend is similar, but the effect of interactions alone differs in magnitude. This difference arises from the distinction between the current interaction and permanent passivation, suggesting that junction formation involves additional changes beyond the interfacial interactions observed here. Our approach consistently isolates and monitors effects arising solely from these interactions.

CCI also modulates phase-transition dynamics. As shown in Fig. 2e, strong CCI (C8N1 and C12N1) suppresses the α-to-δ phase transition in $FAPbI_3$ under accelerated ageing conditions, whereas weaker CCI (C4N1) does not. Since phase transitions typically initiate at the surface, CCI acts as an effective surface constraint. Cage-cation substitution clarifies the mechanism: replacing FA with dipolar methylammonium preserves CCI-induced phase suppression, whereas substitution with non-dipolar Cs prevents CCI activation altogether (Supplementary Fig. 5). In the absence of dipole-induced dipole interactions, CCI fails to impose a surface constraint, and the films readily transition to the δ-phase (Fig. 2f). Notably, Fig. 2g shows that strong CCI (C8N1 and C12N1) suppresses the reverse δ-to-α phase transition in $FAPbI_3$ at 150 °C. Suppression increases with CCI strength and occurs more gradually than α-to-δ transitions. CCI-driven phase-transition suppression is consistently observed across different perovskite frameworks, and bidirectional temperature cycling between room temperature and 150 °C confirms that CCI remains effective throughout the relevant temperature range (Supplementary Figs. 6 and 7 and Supplementary Note 3).

Unique recrystallization through an additional heating process under CCI

The fact that bulk properties remain controlled across a wide temperature range under CCI conditions raises interest in the recrystallization outcomes of $FAPbI_3$ under CCI. We investigated the changes induced by additional heating after establishing a CCI environment with α-phase $FAPbI_3$. When a transparent glass substrate is placed in contact and heated, no CCI occurs, resulting in thermal degradation. Despite the establishment of a CCI with material present at the interface, excessively high temperatures induce mutual material intrusion between the interfaces, even in a simple contact state. This leads to the formation of quasi-2D phases on the 3D perovskite side, hindering the observation of changes driven solely by the interaction. Through experiments involving varying temperatures and 2D types with different CCI strengths, we identified a temperature range where the CCI is maintained without thermal intrusion into the 3D substrate (Extended Data Figs. 2–4 and Supplementary Note 4). Specifically, at the CCI interface between the 3D perovskite and C8N1 heated at 90 °C for 1 h, no material intrusion into the 3D perovskite was observed.

Figure 3a and Extended Data Fig. 5 present in situ PL measurements observed during 90 °C heating under various CCI conditions (Supplementary Note 5). Before annealing, PL signals from the 2D and 3D were observed. Signals corresponding to the quasi-2D phase appear during heating, with their type and quantity depending on the 2D type. When CCI is formed with C4N1, peaks corresponding to $n = 2$ to $n = 4$ appear, but with 2D types possessing longer chains, only the $n = 2$ phase

https://doi.org/10.1038/s41560-026-02027-4

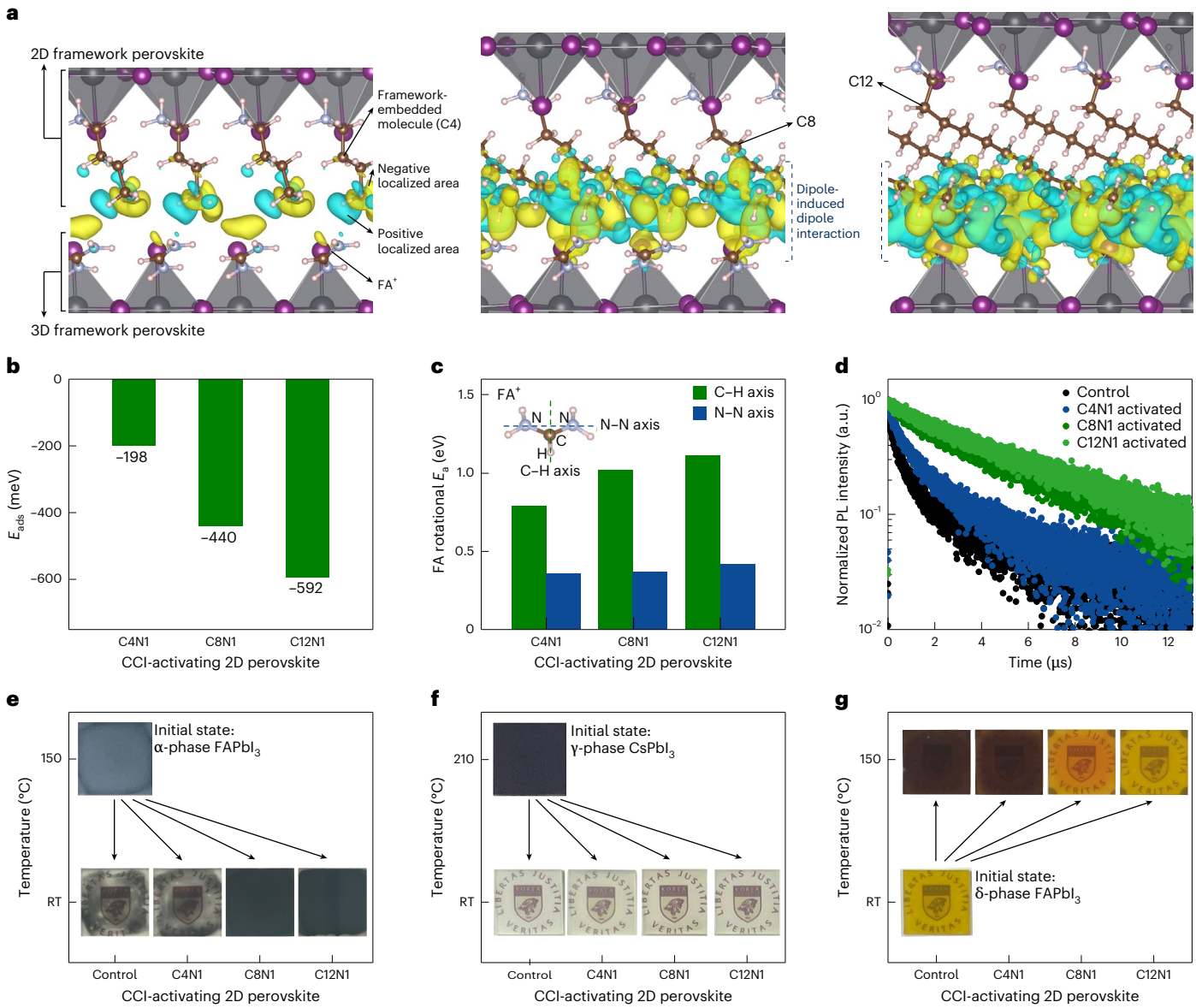

Fig. 2 | Mechanism of CCI and regulation of phase transition. a, DFT-calculated differential charge density maps for CCI at the interface between $FAPbI_3$ and various 2D perovskites. **b**, Adsorption energy (E_{ads}) between $FAPbI_3$ and 2D perovskites under CCI activation. **c**, Correlation between E_{ads} and the rotational energy barrier (E_a) of FA^+ along the C–H and N–N axes under CCI. The inset shows the FA^+ molecular structure and the corresponding rotational axes. **d**, Time-resolved PL decay of $FAPbI_3$ under CCI with different 2D spacers, measured without heat or pressure. Each curve was obtained on the same 3D film under different CCI conditions. **e**, α-to-δ phase transition of $FAPbI_3$ under various CCI conditions. α-phase $FAPbI_3$ films, fabricated at 150 °C, are contacted with different 2D spacers and then exposed to 80% relative humidity at 25 °C for 12 h. **f**, γ-to-δ phase transition of $CsPbI_3$ under various CCI conditions. γ-phase $CsPbI_3$ films, fabricated at 210 °C, are contacted with different 2D spacers and then exposed to 80% relative humidity at 25 °C for 10 min. **g**, δ-to-α phase transition of δ-phase $FAPbI_3$ under various CCI. δ-phase $FAPbI_3$ films undergo CCI with 2D spacers and are then annealed at 150 °C for 10 min. In **e**–**g**, the 3D films were exposed to each condition while stacked with the 2D film, and imaging was performed after separation, without additional pressure. RT, room temperature.

is observed, with no other phases detected. To investigate the state and distribution of these quasi-2D phases, the substrates were detached after 1 h of cooling and ultraviolet (UV)–visible light spectroscopy was performed on each sample. Under CCI with C4N1, the transition to higher n values, such as $n = 4$, occurs only in the 2D layer, whereas in the 3D substrate, only up to $n = 2$ is observed (Supplementary Fig. 8). This finding indicates that material intrusion is not fully controlled during heating under CCI with C4N1. By contrast, for CCIs with 2D types possessing chains longer than C8N1, only up to $n = 2$ is observed in the 2D perovskite substrate after separation, with no 2D signals detected in the 3D substrate (Fig. 3b). These results were additionally corroborated by emission spectra and grazing-incidence X-ray diffraction (XRD) of the detached films (Supplementary Figs. 9 and 10). This finding suggests a unilateral outflow of FA cations in the 3D perovskite, indicating that cation rearrangement may occur under contact with materials, creating stronger CCI conditions. On this basis, the C8N1 interface, which reflects the effect of one-hour heating at 90 °C under CCI, was selected as the representative CCI system for subsequent analyses and is referred to as the CCI-driven group.

To examine changes in the distribution state of FA cations within the film, photo-induced force microscopy (PiFM) was conducted. The inset image in Fig. 3c shows PiF distribution images for control and CCI-driven $FAPbI_3$, based on the wavenumber corresponding to the C=N position in FA. CCI-driven $FAPbI_3$ exhibited a more uniform PiF signal distribution, indicating a more homogeneous FA state across the entire area. Figure 3c illustrates the pixel distribution of the PiF

https://doi.org/10.1038/s41560-026-02027-4

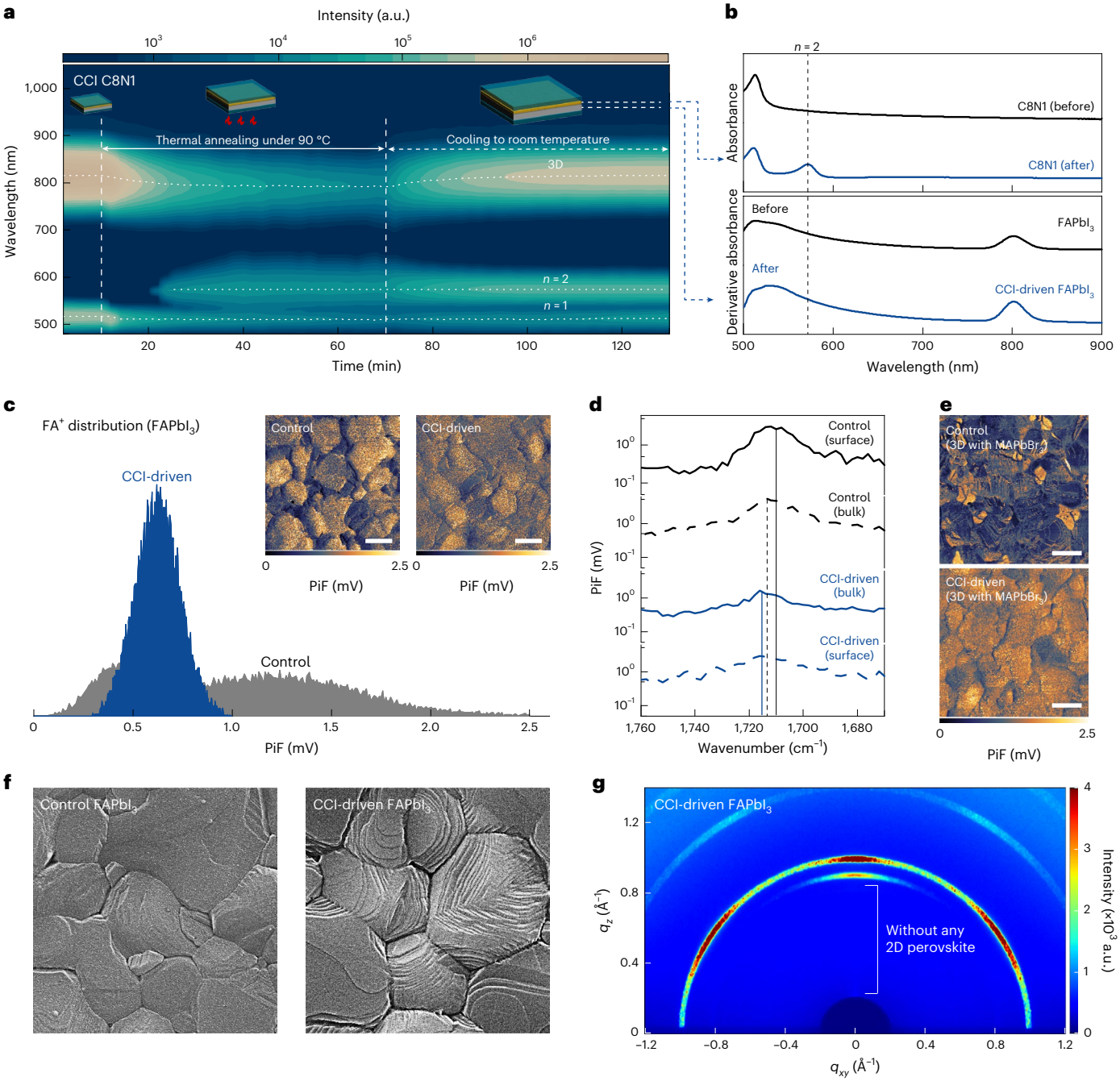

Fig. 3 | Recrystallization through an additional heating process under CCI. a, In situ PL mapping during C8N1-based CCI treatment, where both films are brought into direct contact and annealed at 90 °C. The insets schematically illustrate the stacking configuration of the contacting films during thermal annealing and subsequent cooling to room temperature. **b**, Absorbance and derivative absorbance spectra of C8N1 and $FAPbI_3$ films before and after CCI treatment with C8N1, revealing the emergence of an $n = 2$ quasi-2D feature only after CCI with C8N1. The 2D signature is confined to the C8N1 film and is absent in the 3D $FAPbI_3$ film. **c**, FA^+ distribution in each film measured by PiFM using the characteristic vibrational signal at 1,711 cm^{-1}. The PiFM signal is detected at depths of approximately 100–300 nm. Inserted infrared mapping images show the FA^+ distribution over a 5 μm × 5 μm area; scale bar, 1 μm. **d**, PiF spectra as a function of wavenumber for control and CCI-driven $FAPbI_3$ films. **e**, PiFM mapping images of control and CCI-driven 3D films with a composition of $[FAPbI_3]_{0.95}[MAPbBr_3]_{0.05}$. Scale bar, 1 μm. **f**, Surface morphology of control and CCI-driven $FAPbI_3$ films. Scale bar, 1 μm. **g**, Grazing-incidence wide-angle X-ray scattering pattern of CCI-driven $FAPbI_3$ films obtained at an incidence angle of 0.117°. This pattern shows only 3D perovskite features, with no evidence of 2D phases at the surface.

values from the inset image. The control shows a broad distribution from 0 to 2.5 mV across both the surface and bulk, encompassing two main regions (Supplementary Fig. 11). By contrast, CCI-driven $FAPbI_3$ exhibits a unified distribution with a single peak in the middle, which is consistent across both the surface and the bulk, indicating a simplified and uniform FA state in both the surface direction and the depth direction. Time-of-flight secondary ion mass spectrometry tracing the vertical (out-of-plane) FA distribution further confirms this uniformity (Supplementary Fig. 12). Figure 3d shows the PiF values as a function of the wavenumber for both surface and bulk regions. We tracked the C=N bond stretch near 1,710 cm^{-1}, where the peak shift indicates the strength of cation coupling with the surrounding lattice. A shift to higher wavenumbers suggests stronger bond reinforcement, potentially indicating weaker coupling with the surrounding lattice.

In the control, a difference in peak position exists between the surface and bulk, with a shift to lower wavenumbers towards the surface. However, in the CCI-driven $FAPbI_3$, the peak positions of the surface and bulk are identical and are located at higher wavenumbers than those of the control, indicating looser coupling between FA and the surrounding lattice[44]. These results suggest that CCI-based heating resolves excessive and deficient FA regions, achieving a uniform distribution across the bulk while forming an appropriate coupling state. This interaction-driven recrystallization occurs without introducing additional material and represents a previously unreported remediation pathway. Figure 3e shows the PiFM results for the composition mixed with $FAPbI_3$ and $MAPbBr_3$ at a 95:5 ratio. The PiFM image shows that the uneven distribution of FA in this composition becomes even more extreme, with FA existing in a more clustered state in very bright areas. This finding indicates that the additive material improvement method can worsen the uniformity of the local composition or lattice structure, and these uneven points can complicate material analysis and act as a trigger for performance degradation. By contrast, the CCI-driven group uniformizes the FA distribution in this composition as well. This finding demonstrates that the CCI-based recrystallization process can be effectively applied to perovskite framework combinations with different halides or cations. In all surface and bulk areas, wavenumber shifts, homogenization and resolution of the uneven distribution are observed (Supplementary Figs. 13 and 14). Conventional solution-based passivation does not lead to a comparable level of homogenization (Supplementary Fig. 15), underscoring the distinct nature of CCI-driven remediation.

CCI-driven recrystallization also alters grain morphology. The surface scanning electron microscope images before and after CCI treatment are shown in Fig. 3f. After CCI treatment, the surface of the $FAPbI_3$ grain, which usually has a curved form, exhibits a highlighted stepped form. To perform crystallographic analysis on this form, grazing-incidence wide angle X-ray scattering analysis was conducted. First, in the CCI-driven $FAPbI_3$, no crystallographic signal corresponding to the 2D perovskite is observed (Fig. 3g). In the azimuthal intensity profiles along $(110)_t$, compared with the control, CCI-driven $FAPbI_3$ has better crystallographic orientation uniformity (Extended Data Fig. 6). This improvement extends beyond the surface area to the bulk (Supplementary Note 6 and Supplementary Figs. 16 and 17). These results demonstrate that CCI enables a non-additive recrystallization process, which simultaneously corrects local chemical imbalances and promotes orientation unification. These findings highlight that the strength of interfacial interactions is a critical parameter controlling the structural state of the perovskite framework.

Crystallographic, electrical and chemical properties of CCI-driven $FAPbI_3$

Resolving local compositional imbalances and simplifying crystal orientation enable the fabrication of $FAPbI_3$ with a crystal structure consistent with theoretical expectations. This sparks interest in the crystallographic, electrical and chemical properties of $FAPbI_3$ with sufficiently resolved FA non-uniformity and reoriented crystal alignment achieved through CCI-based heat treatment. Control $FAPbI_3$ refers to pure $FAPbI_3$ without additional CCI-based processing. To investigate changes in the crystallographic properties of the 3D perovskites, XRD analysis was performed (Fig. 4a). Based on prior studies, we assumed a tetragonal lattice structure for the 3D perovskite, and the data were calibrated to match the FTO substrate peaks. The observed XRD peaks for the CCI-driven $FAPbI_3$, including $(110)_t$, $(111)_t$, $(201)_t$, $(220)_t$ and $(310)_t$, shifted to lower angles compared with those of control $FAPbI_3$, accompanied by a reduction in microstrain (Supplementary Figs. 18 and 19). This peak shift, accompanied by morphological changes (Supplementary Fig. 20), occurred progressively depending on the CCI processing temperature and time (Supplementary Figs. 21–24). Progressive peak shift and strain relaxation under CCI conditions indicate that interfacial interactions drive structural refinement of the perovskite framework. This surface-initiated process gradually propagates into the bulk, resulting in permanent lattice-level adjustments. The peak shift indicates lattice expansion, particularly with larger changes in diffraction planes involving the *c*-axis lattice constant. We calculated the theoretically expected lattice constants *a* and *c* for $FA_xMA_{1-x}PbI_3$ ($0.7 \leq x \leq 1$) compositions, marked with dashed lines (Fig. 4b,c). The control samples without CCI-based remediation closely matched the theoretical lattice parameters *a* and *c* when methylammonium was added but exhibited a distinct decrease in the lattice constant with only FA. This is attributed to lattice distortion from microstrain, defects or phase transitions to δ-$FAPbI_3$. Based on prior PiFM measurements, we know that even MA-added compositions matching theoretical values exhibit non-uniform FA distribution; thus, this matching state is interpreted as an average of expanded or contracted regions aligning with theoretical values due to local compositional differences. By contrast, CCI-driven $FAPbI_3$ resolves the sharp decrease in pure $FAPbI_3$, resulting in consistent lattice constants across all tested composition ranges, reflecting the reproduction of the ideal $FAPbI_3$ with a uniform chemical composition and lattice state.

CCI-driven $FAPbI_3$ demonstrates notable improvements in optoelectronic properties. The PL quantum efficiency (PLQE) was measured under 1-sun equivalent open-circuit conditions to assess quality. The CCI-driven $FAPbI_3$ achieved over 50% PLQE, while the PLQE of the control $FAPbI_3$ reached approximately 23% (Fig. 4d). The trends in the carrier lifetime and carrier density align with these results (Supplementary Note 7 and Supplementary Figs. 25 and 26). The mobility and diffusion length under open-circuit conditions increased from approximately 16 $cm^2 V^{-1} s^{-1}$ and 1.6 μm for the control to 22 $cm^2 V^{-1} s^{-1}$ and 2.4 μm for the CCI-driven $FAPbI_3$, respectively (Fig. 4e,f). The diffusion length of CCI-driven $FAPbI_3$ is comparable to that of additive-enhanced $FAPbI_3$ films. Achieving these metrics with the base composition, without complex additive combinations, offers greater process flexibility for long-term technological advancements.

In addition, it is noteworthy that such a CCI-driven $FAPbI_3$ possesses intrinsically excellent phase stability. To accelerate phase stability testing in film form, the fabricated films were exposed to 60% RH, followed by absorbance measurements. The control $FAPbI_3$ transitioned to the δ-phase after 250 h, whereas the CCI-driven $FAPbI_3$ showed no phase transition during the same period (Fig. 4g). In addition, no discernible changes in the PL spectra were observed after 500 h of 1-sun continuous irradiation at 85 °C (Supplementary Fig. 27). Although control $FAPbI_3$ films exhibited a blueshift in the PL peak position, CCI-driven $FAPbI_3$ showed no change in the PL emission position. To measure the intrinsic material stability independent of external strain from the substrates, XRD was performed on perovskite powders scraped after fabrication (Fig. 4h). After 100 h in air, the control $FAPbI_3$ powder transitioned to the δ-phase, whereas the photoactive phase of the CCI-driven $FAPbI_3$ powder was maintained. These stability improvements arise not from a change in the thermodynamic landscape but from the suppression of kinetic δ-phase nucleation pathways. CCI-driven $FAPbI_3$ exhibits substantially reduced internal strain and a more uniform FA distribution, which minimize defect-induced initiation sites for the α-to-δ transition. These improvements in environmental stability and performance are attributed to the resolution of local chemical imbalances, orientation uniformity and optoelectronic material enhancements, directly contributing to device performance.

Device performance and long-term stability of CCI-driven PSCs

CCI-driven $FAPbI_3$ was employed as the absorber layer in PSCs fabricated using a standard architecture with SnO_2 and 2,2′,7,7′-tetrakis(*N*,*N*-di-4-methoxyphenylamine)-9,9′-spirobifluorene (Spiro-OMeTAD) as electron and hole transporting layers, respectively. The best performances for the control and CCI-driven $FAPbI_3$ devices, without any

https://doi.org/10.1038/s41560-026-02027-4

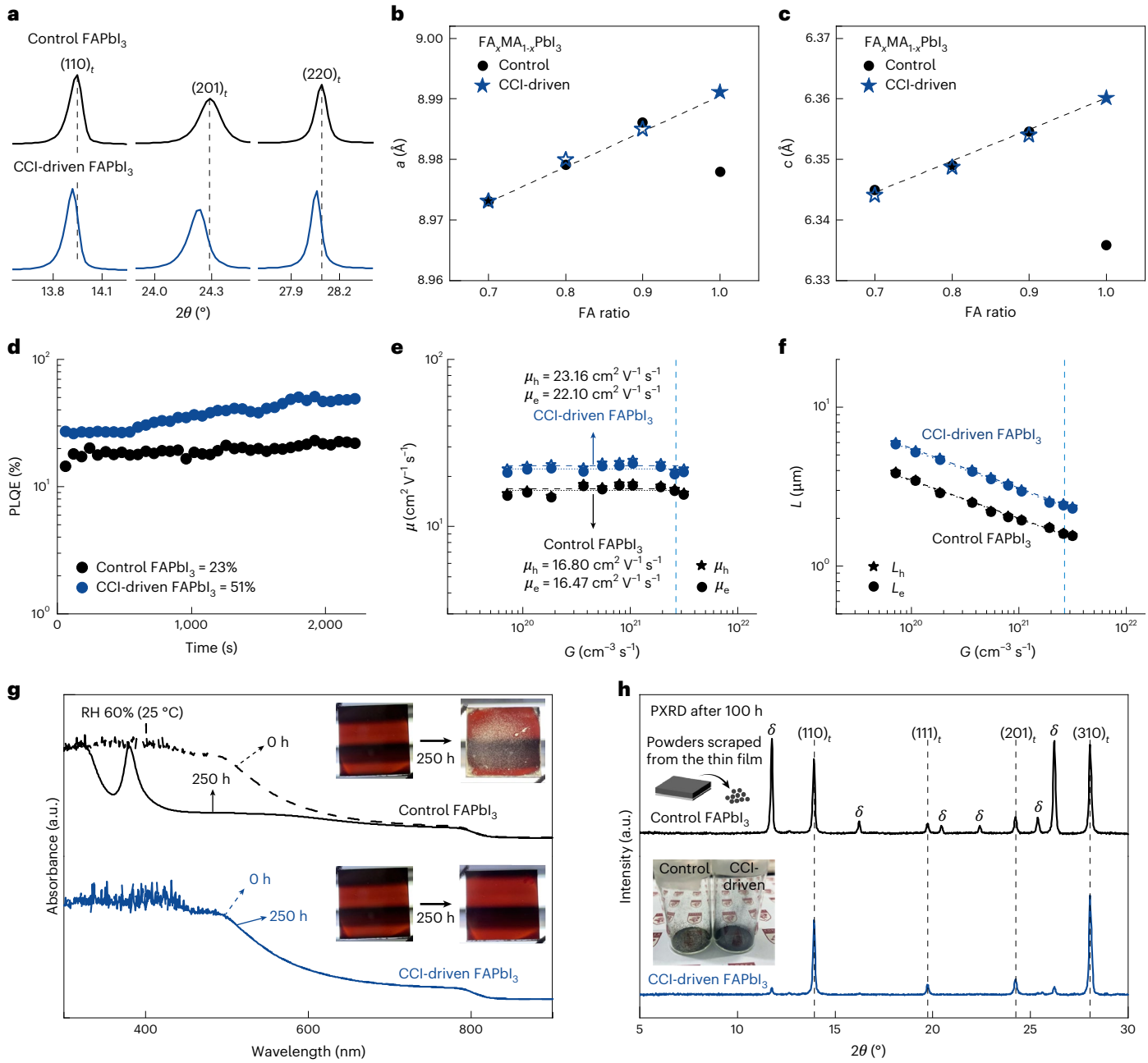

Fig. 4 | Crystallographic, electrical and chemical properties of CCI-driven $FAPbI_3$. **a**, XRD patterns of control and CCI-driven perovskite films, with the (110), (201) and (220) planes indexed to the tetragonal phase. **b**,**c**, Lattice parameters *a* (**b**) and *c* (**c**) as a function of the FA ratio in the $FA_xMA_{1-x}PbI_3$ system ($0.7 \leq x \leq 1$). The black circles indicate perovskite films with various FA/MA ratios prepared by the conventional method, whereas the blue stars represent the CCI-driven 3D perovskite. The dashed curves are guides to the eye. **d**, PLQE as a function of time for control and CCI-driven $FAPbI_3$. **e**, Hole and electron mobilities plotted against absorbed photon density. μ_h and μ_e denote the mobilities of holes and electrons, respectively. **f**, Hole and electron diffusion lengths mapped against absorbed photon density. L_h and L_e denote the diffusion lengths of holes and electrons, respectively. In panels **e** and **f**, the black and blue symbols indicate the values for control and CCI-driven $FAPbI_3$, respectively. The vertical dashed line represents the absorbed photon density corresponding to the 1-sun condition. The dashed curves are guides to the eye. **g**, Accelerated phase-stability test under 60% relative humidity (RH) at 25 °C. The insets show photographs of the perovskite films before and after exposure. The phase-stability test was carried out using perovskite films prepared on 2.5 cm × 2.5 cm substrates. **h**, Powder XRD patterns of powders scraped from each film after 100 h. The schematic inset illustrates the scraping procedure from the thin films, and the photographic insets show the resulting powders after 100 hours of exposure. PXRD, powder X-ray diffraction.

surface passivation, obtained from the current density–voltage (*J*–*V*) curve are displayed in Fig. 5a. In the CCI-driven $FAPbI_3$ device, a PCE of 26.25% was achieved with a short-circuit current density (J_{SC}) of 26.40 mA cm^{-2}, an open-circuit voltage (V_{OC}) of 1.183 V and a fill factor of 84.05% under standard test conditions for solar cells. It also demonstrated a stabilized power output of 25.71% at the maximum power point (Supplementary Fig. 28). This enhancement in performance was achieved by improving all the photovoltaic parameters compared with those of the control device. Moreover, an independent external institution certified a PCE of 25.61% (Supplementary Fig. 29). This performance increase from the CCI-driven $FAPbI_3$ was replicated in PSCs with an expanded active area of 1 cm^2, resulting in a PCE of 24.90% (Supplementary Fig. 30). Using conventional solvent-assisted surface passivation with octylammonium iodide on $FAPbI_3$, the device

https://doi.org/10.1038/s41560-026-02027-4

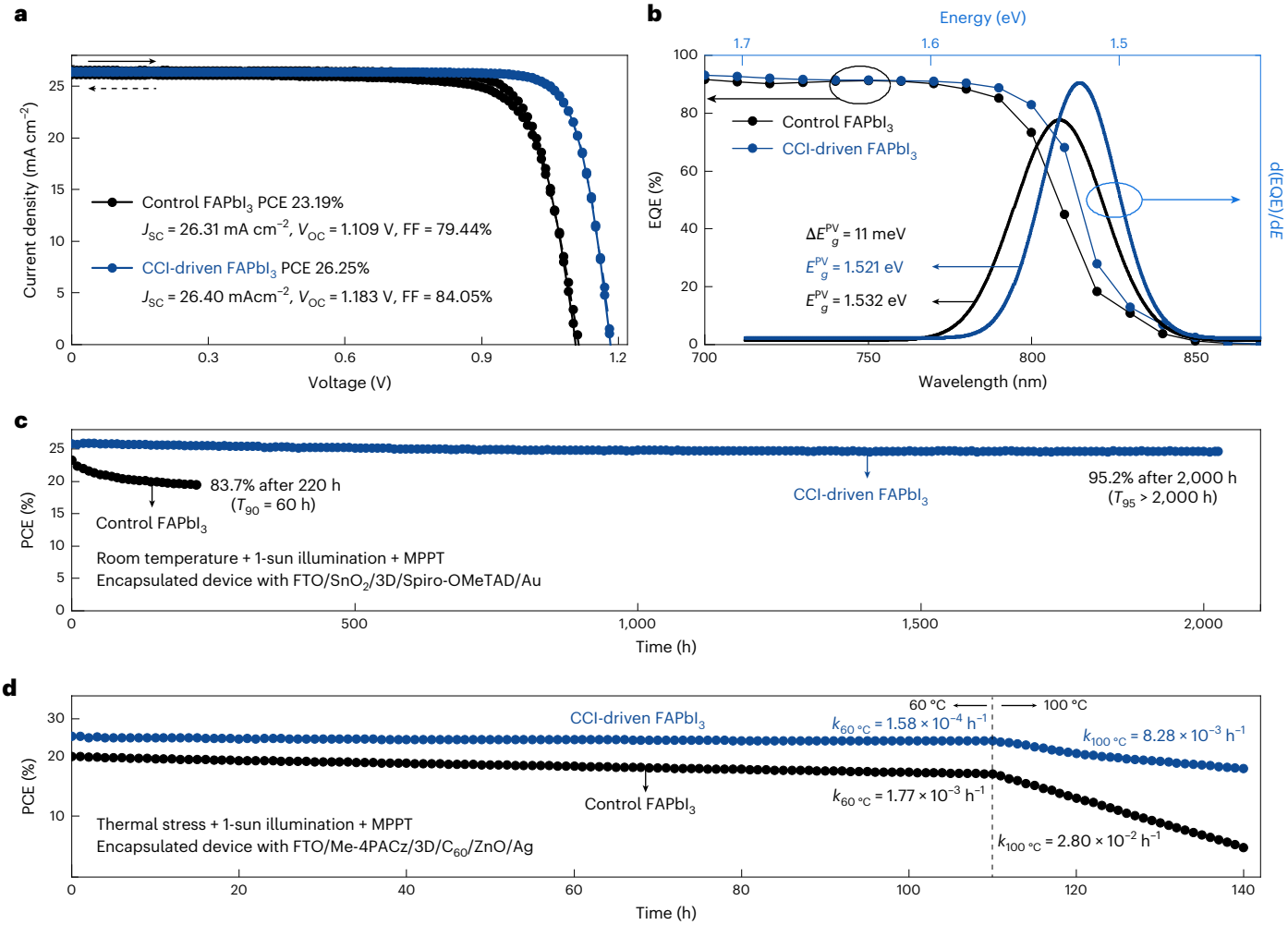

Fig. 5 | Device performance and long-term stability of CCI-driven PSCs. a, J–V curves of PSCs with $FAPbI_3$ and CCI-driven $FAPbI_3$ as light-harvesting layers; the solid and dashed lines represent the reverse and forward scans, respectively. **b**, EQE and photovoltaic bandgap (E_g^{PV}) of $FAPbI_3$ and CCI-driven devices; E_g^{PV} is obtained from d(EQE)/dE, and the difference between devices is presented as ΔE_g^{PV}. **c**, Operational stability of encapsulated PSCs under 1-sun illumination with MPPT at room temperature. T_{80} is defined as the elapsed time at which the PCE decreases to 80% of its initial performance. **d**, Accelerated stability test of encapsulated PSCs under thermal stress (60 °C and 100 °C) and continuous 1-sun illumination with MPPT. Degradation rates at each temperature (k_{60} and k_{100}) indicate the speed of performance loss under thermal and illumination stress. FF, fill factor.

efficiency was improved, but the improvement was limited to a PCE of 24.3% (Supplementary Fig. 31). The stark contrast among the control, surface-only passivation and CCI-driven $FAPbI_3$ demonstrates that the distribution of FA cations has a crucial effect on device performance. Statistical evidence supports the reliability of device performance improvements and trends throughout the process (Supplementary Fig. 32). The CCI-driven 3D process achieves a uniform bulk composition, enabling high efficiencies comparable to those of the best additive methods while addressing challenges related to reproducibility and stability.

The CCI-driven $FAPbI_3$ device exhibited a J_{SC} of 26.40 mA cm^{-2}, as determined by the external quantum efficiency (EQE), attributed to an 11-meV redshift in the photovoltaic bandgap (E_g^{PV}) rather than an improved extraction performance (Fig. 5b). This reduction in E_g^{PV} can be attributed to the variation in the light absorbing material's properties and device structure. The optical bandgap shifts in the CCI-driven $FAPbI_3$ film, arising from lattice expansion and structural modifications, suggest that the E_g^{PV} decrease is primarily related to changes in the material's properties (Supplementary Fig. 33). To detect defects at the device level, the solar cells were operated with light-emitting diodes (LEDs) to measure the external radiation efficiency (ERE). The electroluminescence spectrum was obtained by injecting the current density corresponding to the J_{SC} into each solar cell (Supplementary Fig. 34). The ERE of the CCI-driven $FAPbI_3$ device was 11.71% under standard test conditions, far surpassing the 0.74% ERE of the control device (Supplementary Fig. 35). The results of the V_{OC} loss analysis, which is based on the above EQE and ERE, are shown in Supplementary Fig. 36, confirming that the CCI-driven $FAPbI_3$ device achieves 95.63% of the radiative open-circuit voltage limit ($V_{OC\text{-}rad}$).

We conducted stability tests under various stress conditions, including light and thermal stress. As shown in Fig. 5c, the encapsulated CCI-driven $FAPbI_3$ device maintained 95.2% of its initial PCE of 25.65% during 2,000 h (T_{95} > 2,000 h) of 1-sun illumination at maximum power point tracking (MPPT) and room temperature. By contrast, the device with control $FAPbI_3$ showed a decrease in the PCE to 83.7% of its initial value (23.34%) after only 220 h (T_{90} = 60 h). Moreover, we aimed to determine the operational stability of CCI-driven $FAPbI_3$ by applying thermal stress[45]. Notably, owing to the thermal instability of Spiro-OMeTAD present in the standard structure, PSCs with inverted architectures (FTO/Me-4PACz/control or CCI $FAPbI_3$/C_{60}/ZnO/Au) were used for stability tests under thermal stress[46] (Supplementary Fig. 37). The introduction of thermal stress at 60 °C gradually decreased the performance of the control and CCI-driven $FAPbI_3$, reducing their efficiency to 81.60% and 95.01% of their initial efficiency after 110 h,

respectively, while increasing the thermal stress to 100 °C caused a more severe reduction in efficiency (Fig. 5d). By deriving the degradation rate (k) at each temperature from the respective degree of efficiency decrease, the degradation rates at 60 °C (k_{60}) were 1.77×10^{-3} h^{-1} and 1.58×10^{-4} h^{-1} for the control and CCI-driven $FAPbI_3$, respectively. At 100 °C, the rates (k_{100}) were 2.8×10^{-2} h^{-1} and 8.28×10^{-3} h^{-1} for the control and CCI-driven $FAPbI_3$, respectively. The temperature dependence of the degradation rate yields the activation energies for degradation, which were 0.616 ± 0.021 eV and 0.947 ± 0.013 eV for the control and CCI-driven $FAPbI_3$, respectively (Supplementary Fig. 38). The degradation activation energy of the CCI-driven $FAPbI_3$ device is the highest reported thus far (Supplementary Table 2). Moreover, these accelerated ageing tests provide information about the device lifetime (T_{80}), which corresponds to 80% of the initial efficiency and serves as an indicator of solar cell stability. By calculating the acceleration factor from the temperature-dependent degradation rate, the T_{80} of the CCI-driven $FAPbI_3$ device at room temperature was estimated to be approximately 24,800 h. Notably, this remarkable improvement in device lifetime was derived from remediation of both the bulk and surface of the 3D perovskite, demonstrating that perovskite has the potential to meet market performance requirements for solar cells.

The generalizability of CCI-induced lattice reorganization was further confirmed in narrow-bandgap PbSn perovskite alloys, where the champion device achieved a PCE of 24.45% (Supplementary Fig. 39 and Supplementary Note 8). These findings demonstrate the broad applicability of CCI-driven lattice reorganization to complex perovskite compositions.

Conclusion

This study identifies and quantifies interfacial molecular interactions that arise under simple contact between framework-structured perovskites. Cations and Pb–I octahedra within the perovskite framework interact through mere physical contact, reversibly modulating PL and phase transition behaviour. Dipole cations experience rotational constraints imposed by the opposing interface. Additional heating under CCI condition triggers a previously unreported mode of 3D perovskite recrystallization. Without permanent additives of 2D/3D junction formation, CCI-annealing achieves a uniform FA cation distribution throughout the 3D bulk, reduced lattice orientation dispersion and lattice parameters aligned with theoretical values. As a result, CCI-driven $FAPbI_3$ exhibit a PLQE exceeding 50% enabled by enhanced carrier mobility and lifetime, together with markedly improved optical, thermal and chemical stability. Solar cells utilizing CCI-driven $FAPbI_3$ achieve a PCE of 26.25% and a projected operational lifetime exceeding 20,000 h. These findings demonstrate that simple physical contact not only modulates the optoelectronic properties but also triggers unconventional recrystallization in halide perovskites. The phenomena uncovered here point towards device functionalities enabled by engineered contact molecular interactions in framework-structured materials.

Methods

Materials

Urea, potassium chloride (KCl, 99.999%), thioglycolic acid, hydrochloric acid (HCl, 37%), *N*,*N*-dimethylformamide (DMF, 99.8%), dimethyl sulfoxide (DMSO, ≥99.9%), acetonitrile (ACN, 99.8%), chlorobenzene (CB, 99.8%), bis(trifluoromethane)sulfonimide lithium salt (Li-TFSI, 99.95%), 4-*tert*-butylpyridine (98%), zinc oxide (ZnO), tin(II) iodide (SnI_2), tin(II) fluoride (SnF_2), bathocuproine, glycine hydrochloride, C_{60}, [6,6]-phenyl-C_{61}-butyric acid methyl ester (PCBM) and nanoparticle ink solution were purchased from Sigma Aldrich. FA iodide (>99.99%), methylammonium iodide, methylammonium chloride (MACl, >99.99%) and *n*-octylammonium iodide (>99%) were purchased from Greatcell solar. 2,2′,7,7′-tetrakis[*N*,*N*-di(4-methoxyphenyl)amino]-9,9′-spirobifluorene (spiro-OMeTAD) and tris(2-(1*H*-pyrazol-1-yl)-4-*tert*-butylpyridine)cobalt(III) tri[bis-(trifluoromethane)]sulfonamide (FK209) were purchased from Lumtec. Lead(II) iodide (99.99%), [4-(3,6-dimethyl-9*H*-carbazol-9-yl) butyl]phosphonic acid (Me-4PACz), ethane-1,2-diammonium iodide ($EDAI_2$) and guanidine thiocyanate (GuaSCN) were purchased from the Tokyo Chemical Industry. $SnCl_2{\cdot}2H_2O$, 2-methoxyethanol (2-Me, 99%+) was purchased from Alfa Aesar. Diethyl ether (99.5%) was purchased from SAMCHUN. Poly(3,4-ethylenedioxythiophene) polystyrene sulfonate (PEDOT:PSS; Al 4083) were purchased from Ossila.

$FAPbI_3$ micro powder synthesis

The black-phase $FAPbI_3$ micro powder was synthesized in accordance with previously published protocols[4,47]. Specifically, the micro powder was synthesized by using 0.8 M precursor solution containing FA iodide and PbI_2 in 33 ml of 2-Me. The precursor solution with stirring bar was heated to 120 °C in an oil bath and then precipitated using the retrograde method for 3 h. The filtered $FAPbI_3$ micro powder was baked at 150 °C for 30 min.

C8N1 2D micro powder synthesis

A mixed solution of HI solution (16 ml) and H_3PO_2 solution (2 ml) was prepared in a 200-ml glass volumetric flask. PbO powder (2,232 mg, 10 mmol) was dissolved by heating to boiling under stirring, and it formed a bright yellow solution; 1,669 µl (10 mmol) of octylamine was then added to this solution and stirring was discontinued. The temperature was lowered to 80 °C over 30 min. The solution was left at room temperature until orange crystals began to form. The crystals were isolated by suction filtration and thoroughly dried in a vacuum chamber.

2D perovskite thin film fabrication

ITO substrates of 2.5 cm × 2.5 cm were sequentially washed with deionized water, acetone, and 2-propanol for 15 min each. The substrates were then cleaned with UV/O_3 for 15 min for better wetting of the 2D perovskite precursor solution. 0.2 M $(R)_2PbI_4$ (where R is C4, C8, or C12) precursor solution was prepared by dissolving in DMSO and DMF with a volume ratio of 1:8. The precursor solution was then spin-coated on the substrate at 5,000 rpm (acceleration 5,000 rpm s^{-1}) for 20 s; 1 ml of diethyl ether was quickly poured onto the substrate at 10 s. Then, the 2D perovskite film was transferred to a hot plate and heat-treated at 80 °C for 5 min. For the PbSn devices, an $EDAPbI_4$ precursor solution with a concentration of 0.2 M was prepared by dissolving $EDAI_2$ and PbI_2 in a 1:1 molar ratio in a mixed solvent of DMF and DMSO (8:1, v/v). The precursor was then spin-coated onto ITO substrates at 6,000 rpm (acceleration 6,000 rpm s^{-1}) for 30 s, and 1 ml of diethyl ether was quickly dripped onto the substrate 10 s before the end of the spin-coating step. The films were subsequently annealed at 100 °C for 5 min. We recommend that the 2D perovskite film be produced at 30–40% relative humidity.

Electron transport layer fabrication for n–i–p architecture device

Prepatterned Ashahi FTO substrates were cleaned with deionized water, acetone, ethanol and 2-propanol for 15 min, respectively. The substrates were then treated with UV/O_3 for 30 min before tin oxide (SnO_2) deposition. 10 mM of $SnCl_2{\cdot}2H_2O$ with 10 g of urea was dissolved in 200 µl of thioglycolic acid, 10 ml of HCl and 800 ml of deionized water. FTO substrate was dipped in the solution at 90 °C for 6 h according to previous reports[2,48]. The substrates for depositing SnO_2 were then heat-treated at 150 °C for 6 h.

Hole transport layer fabrication for p–i–n device

Prepatterned Ashahi FTO substrates were cleaned with deionized water, acetone, ethanol and 2-propanol for 15 min, respectively. The substrates were then treated with UV/O_3 for 60 min. A total of 0.1 ml of Me-4PACz solution (0.4 mg ml^{-1} in ethanol) was loaded onto the

substrate and coated at 3,000 rpm (acceleration 3,000 rpm s^{-1}) for 30 s. Then, the Me-4PACz coated substrate was heat-treated at 120 °C for 10 min. This process was repeated twice to ensure device reproducibility. For the PbSn devices, PEDOT:PSS diluted with deionized water at a 1:4 volume ratio was spin-coated onto FTO substrates at 6,000 rpm for 40 s, followed by thermal annealing at 120 °C for 20 min. The substrates were then immediately transferred to a nitrogen-filled glovebox after annealing.

3D thin film fabrication for n–i–p device

The FTO/SnO_2 substrates were cleaned by UV–ozone for a further 15 min. KCl solution (30 mM KCl in deionized water) was spin-coated on the FTO/SnO_2 substrate at 5,000 rpm (acceleration 2,500 rpm s^{-1}) for 30 s. Then, the substrate was annealed at 150 °C for 10 min. A total of 1.8 M perovskite precursor solution with the composition of $FAPbI_3$ was prepared by dissolving 1.317 g (2.08 mmol) of $FAPbI_3$ and 0.0492 g (0.728 mmol) of MACl in 1.01 ml (0.951 g) of DMF and 0.15 ml (0.1625 g, 2.08 mmol) of DMSO. Then, 70 µl of the precursor solution was dropped and spin-coated on the FTO/SnO_2 substrate through a two-step spin-coating procedure with 1,000 rpm (acceleration 1,000 rpm s^{-1}) for 5 s and 5,000 rpm (acceleration 1,000 rpm s^{-1}) for 10 s. A total of 1 ml of diethyl ether was quickly poured on the substrate 1 s before the second step end. The yellow film was quickly transferred to a hot plate and annealed at 120 °C for 100 min.

3D thin film fabrication for p–i–n device

Al_2O_3 dispersion solution (0.2 wt%) was spin-coated on the FTO/Me-4PACz substrate at 3,000 rpm for 30 s. Then, the substrate was annealed at 120 °C for 5 min. A total of 1.8 M perovskite precursor solution with the composition of $FAPbI_3$ was prepared by dissolving 1.317 g (2.08 mmol) of $FAPbI_3$ and 0.0421 g (0.624 mmol) of MACl in 1.01 ml (0.951 g) of DMF and 0.15 ml (0.1625 g, 2.08 mmol) of DMSO. Then, 70 µl of the precursor solution was dropped and spin-coated on the FTO/Me-4PACz substrate through a two-step spin-coating procedure with 1,000 rpm (acceleration 1,000 rpm s^{-1}) for 5 s and 5,000 rpm (acceleration 1,000 rpm s^{-1}) for 10 s. A total of 0.1 ml of CB was quickly poured on the substrate 1 s before the second step end. The yellow film was quickly transferred to a hot plate and annealed at 120 °C for 100 min. For the PbSn device, a 2.2-M $[FASnI_3]_{0.6}[MAPbI_3]_{0.4}$ precursor solution was prepared in a mixed solvent of DMF and DMSO with a 4:1 volume ratio. SnF_2 (5 mol% with respect to SnI_2), GuaSCN (7 mol% with respect to methylammonium iodide) and glycine hydrochloride (2 mol% with respect to the total Sn and Pb) were added as additives, and the solution was stirred at room temperature for 2 h. The PbSn perovskite films were then deposited on PEDOT:PSS-coated substrates by spin-coating at 1,000 rpm for 10 s and 4,000 rpm for 30 s, during which 0.5 ml of toluene was dripped onto the substrate 20 s before the end of the second step. The resulting perovskite films were annealed at 100 °C for 10 min.

Fabrication of CCI-driven 3D perovskite

The previously fabricated C8N1 or C12N1 thin film was placed on the 3D perovskite thin film so that the two surfaces were in contact. The stacked films were moved on the hot plate to supply heat towards the 2D direction, and then the balance weight (100 g) was placed on the stacked films. For CCI-driven 3D PbSn perovskite, the 2D perovskite was replaced with $EDAPbI_4$, and the same procedure was conducted in a nitrogen-filled glovebox.

Hole transport layer and counter electrode fabrication for n–i–p device

The Spiro-OMeTAD solution was prepared by adding 23 µl of Li-TFSI solution (540 mg ml^{-1} in ACN), 10 µl of FK209 solution (376 mg ml^{-1} in ACN) and 39 µl of 4-*tert*-butylpyridine to 100 mg of spiro-OMeTAD in 1.1 ml of CB. The Spiro-OMeTAD was deposited by dynamic spin coating on the $FAPbI_3$ and CCI-driven $FAPbI_3$ at 2,000 rpm for 30 s. Finally, the gold electrode was deposited by thermal evaporation. The deposition area of the counter electrode was fixed at 0.16 cm^2.

Electron transport layer and counter electrode fabrication for p–i–n device

The C_{60}/ZnO bilayer was used as the electron transport layer in the inverted structure[46]. First, a 20-nm-thick layer of C_{60} was formed by thermal evaporation. For ZnO layer, ZnO nanoparticle ink was diluted with 2-propanol, coated at 3,000 rpm for 30 s and annealed at 80 °C for 5 min. Finally, the silver electrode was deposited by thermal evaporation. In the PbSn device fabrication, a PCBM solution (7.5 mg ml^{-1}) was deposited onto the PbSn perovskite layer by spin-coating at 5,000 rpm for 50 s and then annealed at 100 °C for 5 min. After the substrates were cooled to room temperature, C_{60} (15 nm) and bathocuproine (8 nm) layers were sequentially formed by thermal evaporation at 0.1–0.3 Å s^{-1}. Finally, a 130-nm Cu electrode was thermally evaporated at a deposition rate of 3.0 Å s^{-1}. The deposition area of the counter electrode was fixed at 0.16 cm^2.

Characterization

The film morphologies were obtained by using a field-emission scanning electron microscope (Hitachi, S-4800). XRD was performed using a Rigaku SmartLab X-ray diffractometer with an X-ray tube (copper Kα, λ = 1.54 Å, 200 mA, 45 kV, 9 kW) at the National Center for Inter-university Research Facilities at Seoul National University. All XRD curves were measured under a scan rate 1° per minute with a step of 0.02°. Standard material (LaB_6) was performed to confirm the instrument broadening. The values of full width at half-maximum were adjusted by using the instrumental broadening according to the previous report[49]. The optical absorbance properties of the films were measured using UV–Vis–near-infrared spectrophotometer (Agilent, Cary 5000). To obtain the *J*–*V* PCE, the devices were measured using a solar simulator (Newport, 94043A) with a source meter (Keithley 2400). The light intensity with AM1.5G illumination was adjusted using a calibrated reference cell (Newport, KG with quartz and KG3). *J*–*V* PCEs were measured from −0.2 V to 1.2 V at 100 mV s^{-1} and 10-mV step intervals. All devices were covered with a metal mask, fixing the active area to 0.096 cm^2. External quantum efficiencies were measured from 320 nm to 900 nm at 10-nm intervals (Newport, QuantX-300). Stabilized power outputs were obtained using a potentiostat (IviumStat.h).

Computational method

The DFT calculations were performed using the VASP code with projector augmented-wave pseudopotentials[50,51]. A plane-wave cutoff of 600 eV and a 3 × 3 × 1 *k*-point mesh were adopted. The Perdew–Burke–Ernzerhof functional was used to describe exchange–correlation interactions[52], whereas van der Waals forces were accounted for using Grimme's D3 correction[53]. All residual atomic forces were converged to below 0.02 eV $Å^{-1}$ during structural relaxation. The 3D crystal structure of the perovskite was visualized using the VESTA software[54].

Grazing-incidence wide-angle X-ray scattering measurement

The grazing-incidence XRD measurements were conducted at the PLS-II 6D beamline of Pohang Accelerator Laboratory in Korea. The X-rays emitted from the bending magnet were monochromatized to 18.986 keV (λ = 0.6530 Å) using a double-crystal monochromator and focused both vertically and horizontally using a sagittal Si(111) crystal and toroidal mirror. The grazing-incidence wide-angle XRD patterns were recorded with a 2D X-ray charge-coupled device detector (MX 225-HS, Rayonix). The incidence angles of 0.117°, 0.145°, 0.3°, 0.483° and 0.8° were used for investigating the penetration depth dependency of perovskite films. The diffraction angles were calibrated using LaB_6 (standard reference material 660c, National Institute of Standards and Technology), and the sample-to-detector distance was ~240 mm. The 2D grazing-incidence wide-angle XRD images were

converted to one-dimensional q_x or q_z profiles using a MATLAB-based homemade program.

PiFM measurements

PiFM data were obtained under ambient conditions using a VistaScope AFM platform, manufactured by Molecular Vista, exploiting a QCL laser (760–1,860 cm^{-1}). The technique provides simultaneous topographic and vibrational spectroscopy information. In the experiments reported here, the sample was mapped at 1,711 cm^{-1} characteristic of the C=N stretching band of the FA ion. The 'bulk' region was scanned with direct detection mode which samples a depth of up to ~300 nm, where the cantilever is actuated at its primary resonance frequency v1, whereas the repetition rate of the stimulating laser is adjusted to correspond to the secondary resonance frequency v2. The 'surface' region was scanned using sideband mode detection which samples a depth of ~20–30 nm, wherein the second driving force is modulated to a 'beat' frequency, which corresponds to the difference or sum of the two mechanical resonances as v1 − v2 (or v1 + v2).

Absolute PLQE measurement

The PLQE and PL spectrum were obtained a 3.2-inch integrating sphere (Horiba, FL-sphere), a fluorometer (Horiba, Fluorolog-3), continuous wave mode of diode laser with 485 nm (Horiba, DeltaDiode-485L-CW) at a continuous power density of 73 $mWcm^{-2}$ (excitation density of 1.8×10^{18} cm^{-3}). The focus area of the laser was confirmed using a laser beam profiler (Newport, LBP2-HR-VIS3). The emission light was collected with a double grating monochromator (Horiba, FL-1005) and a liquid-nitrogen-cooled low-noise photomultiplier tube (Hamamatsu, R5509-43). The absolute PLQE was calculated through the PL spectrum under three conditions: (1) reference laser intensity condition, (2) indirect excitation condition and (3) direct excitation condition[55].

Time-resolved PL measurement

PL decays were obtained time-correlated single-photon-counting method using the double grating monochromator (Horiba, FL-1005) and the liquid-nitrogen-cooled low-noise photomultiplier tube (Hamamatsu, R5509-43). To excite the perovskite film, the pulsed mode of a diode laser with 485 nm (Horiba, DeltaDiode-485L-CW) was used at a fluence of 1.49 nJ cm^{-2} and a repetition rate of 62.5 kHz.

PHEM

The photo-Hall effect measurement (PHEM) specimens were prepared using a prepatterned ITO substrate according to the previous report[56]. All specimens were encapsulated with edge sealing type using 1.1 mm glass and UV-curing resin (Three Bond, 3052B), which was cured under a UV lamp with peak emission at 365 nm (KJUV, KJUV-HS-05). PHEM was measured using a customized PHEM system, which consists of a Hall effect measurement system (ECOPIA, HS7000) with a magnet kit (353 T), 100 W LED with 465 nm and source meter unit (Keithley 2450). An optical power meter (Newport, 1919-R) was used to calculate the absorbed photon density at each light intensity. To control the change of light intensity, the temperature of the LED was maintained through a thermoelectric device. At every light intensity, voltage signals were measured, and then photoconductivity and Hall coefficient were calculated using van der Pauw method. To obtain transport parameters of each carrier, carrier-resolved photo-Hall effect analysis was used, and the final transport parameters were extracted from initial transport parameters using a generalized $\triangle\mu$ model[57,58]. The mobility values were obtained by fitting the experimental data according to established models, assuming constant mobility for holes and electrons in Fig. 4e, following precedent in the literature[57].

Electroluminescence quantum efficient measurement

The electroluminescence spectrum was obtained using the double grating monochromator (Horiba, FL-1005), the liquid-nitrogen-cooled low-noise photomultiplier tube (Hamamatsu, R5509-43), the 3.2-inch integrating sphere (Horiba, FL-sphere) and the source meter unit (Keithley 2450) under injection current density, which corresponded to extracted from the device in the standard test condition. Electroluminescence quantum efficients were measured by directly attaching a calibrated silicon photodiode (Hamamatsu, S1227-1010BQ), which was large collection area than the active area of device. The inject current of the source meter unit (Keithley 2450) and the detected photocurrent of the photodiode were controlled and measured using the software 'SweepMe!'[59].

Device stability test measurement

For the operating test, all devices were encapsulated using 1.1-mm cover glass, polyisobutylene (PIB) tape and UV-curing resin (Three Bond, 3052B). First, the corners of the device, which does not operate as the solar cell, were removed with 2-Me. PIB tape was placed between the device and the cover glass, and the pressure was applied to proceed with the primary encapsulation. Second, edges of device were covered with the resin. The operational tests were performed using a self-customized system and LED solar simulator (Newport, LSH-7320). MPPT was measured using a source meter (Keithley 2450). Every hour, the current from the maximum power point was tracked. The thermal stress under illumination test was performed using device on a hot plate for heat supply.

Reporting summary

Further information on research design is available in the Nature Portfolio Reporting Summary linked to this article.

Data availability

All data generated or analysed during this study are included within the Article and its Supplementary Information. Source data are provided with this paper.

References

1. Jeon, N. J. et al. Compositional engineering of perovskite materials for high-performance solar cells. *Nature* **517**, 476–480 (2015).
2. Yoo, J. et al. Efficient perovskite solar cells via improved carrier management. *Nature* **590**, 587–593 (2021).
3. Kim, G. et al. Impact of strain relaxation on performance of α-formamidinium lead iodide perovskite solar cells. *Science* **370**, 108–112 (2020).
4. Min, H. et al. Efficient, stable solar cells by using inherent bandgap of α-phase formamidinium lead iodide. *Science* **366**, 749–753 (2019).
5. Jeon, N. J. et al. Solvent engineering for high-performance inorganic–organic hybrid perovskite solar cells. *Nat. Mater.* **13**, 897–903 (2014).
6. Kim, D. H. et al. Bimolecular additives improve wide-band-gap perovskites for efficient tandem solar cells with CIGS. *Joule* **3**, 1734–1745 (2019).
7. Yang, S. et al. Stabilizing halide perovskite surfaces for solar cell operation with wide-bandgap lead oxysalts. *Science* **365**, 473–478 (2019).
8. Noh, J. H., Im, S. H., Heo, J. H., Mandal, T. N. & Seok, S. I. Chemical management for colorful, efficient, and stable inorganic–organic hybrid nanostructured solar cells. *Nano Lett.* **13**, 1764–1769 (2013).
9. Tong, J. et al. Carrier lifetimes of > 1 μs in Sn-Pb perovskites enable efficient all-perovskite tandem solar cells. *Science* **364**, 475–479 (2019).
10. Cao, D. H., Stoumpos, C. C., Farha, O. K., Hupp, J. T. & Kanatzidis, M. G. 2D homologous perovskites as light-absorbing materials for solar cell applications. *J. Am. Chem. Soc.* **137**, 7843–7850 (2015).

11. Tsai, H. et al. High-efficiency two-dimensional Ruddlesden–Popper perovskite solar cells. *Nature* **536**, 312–316 (2016).
12. Lee, J.-W. et al. Tuning molecular interactions for highly reproducible and efficient formamidinium perovskite solar cells via adduct approach. *J. Am. Chem. Soc.* **140**, 6317–6324 (2018).
13. Yang, W. S. et al. High-performance photovoltaic perovskite layers fabricated through intramolecular exchange. *Science* **348**, 1234–1237 (2015).
14. Xiang, W. et al. Intermediate phase engineering of halide perovskites for photovoltaics. *Joule* **6**, 315–339 (2022).
15. Zhu, P. et al. Aqueous synthesis of perovskite precursors for highly efficient perovskite solar cells. *Science* **383**, 524–531 (2024).
16. McMeekin, D. P. et al. Intermediate-phase engineering via dimethylammonium cation additive for stable perovskite solar cells. *Nat. Mater.* **22**, 73–83 (2023).
17. Sidhik, S. et al. Two-dimensional perovskite templates for durable, efficient formamidinium perovskite solar cells. *Science* **384**, 1227–1235 (2024).
18. Wang, M. et al. Ammonium cations with high p K a in perovskite solar cells for improved high-temperature photostability. *Nat. Energy* **8**, 1229–1239 (2023).
19. Jung, E. H. et al. Efficient, stable and scalable perovskite solar cells using poly (3-hexylthiophene). *Nature* **567**, 511–515 (2019).
20. Jiang, X. et al. Isomeric diammonium passivation for perovskite–organic tandem solar cells. *Nature* **635**, 860–866 (2024).
21. Wang, Y. et al. Homogenized contact in all-perovskite tandems using tailored 2D perovskite. *Nature* **635**, 867–873 (2024).
22. Sidhik, S. et al. Deterministic fabrication of 3D/2D perovskite bilayer stacks for durable and efficient solar cells. *Science* **377**, 1425–1430 (2022).
23. Ramakrishnan, S. et al. Phase-stabilized 2D/3D hetero-bilayers via lattice matching for efficient and stable inverted solar cells. *Joule* **9**, 101954 (2025).
24. Li, N. et al. Liquid medium annealing for fabricating durable perovskite solar cells with improved reproducibility. *Science* **373**, 561–567 (2021).
25. Li, S. et al. Coherent growth of high-Miller-index facets enhances perovskite solar cells. *Nature* **635**, 874–881 (2024).
26. Turkay, D. et al. Synergetic substrate and additive engineering for over 30%-efficient perovskite-Si tandem solar cells. *Joule* **8**, 1735–1753 (2024).
27. Fei, C. et al. Lead-chelating hole-transport layers for efficient and stable perovskite minimodules. *Science* **380**, 823–829 (2023).
28. Macpherson, S. et al. Local nanoscale phase impurities are degradation sites in halide perovskites. *Nature* **607**, 294–300 (2022).
29. Lee, S. et al. Deciphering 2D perovskite's role in perovskite solar cells via intact 3D/2D junctions. *Energy Environ. Sci.* **17**, 6234–6244 (2024).
30. Jang, Y.-W. et al. Intact 2D/3D halide junction perovskite solar cells via solid-phase in-plane growth. *Nat. Energy* **6**, 63–71 (2021).
31. Xue, J. et al. Crystalline liquid-like behavior: surface-induced secondary grain growth of photovoltaic perovskite thin film. *J. Am. Chem. Soc.* **141**, 13948–13953 (2019).
32. Deumel, S. et al. High-sensitivity high-resolution X-ray imaging with soft-sintered metal halide perovskites. *Nat. Electron.* **4**, 681–688 (2021).
33. Shrestha, S. et al. High-performance direct conversion X-ray detectors based on sintered hybrid lead triiodide perovskite wafers. *Nat. Photon.* **11**, 436–440 (2017).
34. Chen, S. et al. Identifying the soft nature of defective perovskite surface layer and its removal using a facile mechanical approach. *Joule* **4**, 2661–2674 (2020).
35. Kedia, M. et al. Light makes right: laser polishing for surface modification of perovskite solar cells. *ACS Energy Lett.* **8**, 2603–2610 (2023).
36. Lim, J. et al. Efficient charge separation at localized 2D ferroelectric domains in perovskite solar cells. *Energy Environ. Sci.* **18**, 5287–5297 (2025).
37. Mathew, P. S. & Kamat, P. V. Cation migration in physically paired 2D and 3D lead halide perovskite films. *Adv. Opt. Mater.* **12**, 2300957 (2024).
38. Jiang, N. et al. Transfer-imprinting-assisted growth of 2D/3D perovskite heterojunction for efficient and stable flexible inverted perovskite solar cells. *Nano Lett.* **23**, 6116–6123 (2023).
39. Luo, C. et al. Solid–solid chemical bonding featuring targeted defect passivation for efficient perovskite photovoltaics. *Energy Environ. Sci.* **16**, 178–189 (2023).
40. Grancini, G. & Nazeeruddin, M. K. Dimensional tailoring of hybrid perovskites for photovoltaics. *Nat. Rev. Mater.* **4**, 4–22 (2019).
41. Cho, S. H. et al. Fabrication strategies for 2D halide perovskite towards next-generation optoelectronic applications. *Int. J. Precis. Eng. Manuf. Green Technol.* **12**, 349–380 (2025).
42. Gélvez-Rueda, M. C. et al. Effect of cation rotation on charge dynamics in hybrid lead halide perovskites. *J. Phys. Chem. C* **120**, 16577–16585 (2016).
43. Hiraishi, M. et al. Photo-excited charge carrier lifetime enhanced by slow cation molecular dynamics in lead iodide perovskite FAPbI3. *J. Appl. Phys.* **134**, 055106 (2023).
44. Nishida, J., Alfaifi, A. H., Gray, T. P., Shaheen, S. E. & Raschke, M. B. Heterogeneous cation–lattice interaction and dynamics in triple-cation perovskites revealed by infrared vibrational nanoscopy. *ACS Energy Lett.* **5**, 1636–1643 (2020).
45. Zhao, X. et al. Accelerated aging of all-inorganic, interface-stabilized perovskite solar cells. *Science* **377**, 307–310 (2022).
46. Tang, H. C. et al. Reinforcing self-assembly of hole transport molecules for stable inverted perovskite solar cells. *Science* **383**, 1236–1240 (2024).
47. Jeong, J. et al. Pseudo-halide anion engineering for α-FAPbI3 perovskite solar cells. *Nature* **592**, 381–385 (2021).
48. Anaraki, E. H. et al. Highly efficient and stable planar perovskite solar cells by solution-processed tin oxide. *Energy Environ. Sci.* **9**, 3128–3134 (2016).
49. Zhao, Y. et al. Suppressing ion migration in metal halide perovskite via interstitial doping with a trace amount of multivalent cations. *Nat. Mater.* **21**, 1396–1402 (2022).
50. Blöchl, P. E. Projector augmented-wave method. *Phys. Rev. B* **50**, 17953–17979 (1994).
51. Kresse, G. & Furthmüller, J. Efficient iterative schemes for ab initio total-energy calculations using a plane-wave basis set. *Phys. Rev. B* **54**, 11169–11186 (1996).
52. Perdew, J. P., Burke, K. & Ernzerhof, M. Generalized gradient approximation made simple. *Phys. Rev. Lett.* **77**, 3865–3868 (1996).
53. Grimme, S., Antony, J., Ehrlich, S. & Krieg, H. A consistent and accurate ab initio parametrization of density functional dispersion correction (DFT-D) for the 94 elements H-Pu. *J. Chem. Phys.* **132**, 154104 (2010).
54. Momma, K. & Izumi, F. VESTA 3 for three-dimensional visualization of crystal, volumetric and morphology data. *J. Appl. Crystallogr.* **44**, 1272–1276 (2011).
55. Goetz, K. P., Taylor, A. D., Paulus, F. & Vaynzof, Y. Shining light on the photoluminescence properties of metal halide perovskites. *Adv. Funct. Mater.* **30**, 1910004 (2020).
56. Lee, S. & Noh, J. H. Steady-state transporting properties of halide perovskite thin films under 1 sun through photo-Hall effect measurement. *J. Phys. Chem. C* **126**, 9559–9566 (2022).

57. Euvrard, J., Gunawan, O. & Mitzi, D. B. Impact of PbI_2 passivation and grain size engineering in $CH_3NH_3PbI_3$ solar absorbers as revealed by carrier-resolved photo-Hall technique. *Adv. Energy Mater.* **9**, 1902706 (2019).
58. Gunawan, O. et al. Carrier-resolved photo-Hall effect. *Nature* **575**, 151–155 (2019).
59. Cho, C. et al. Effects of photon recycling and scattering in high-performance perovskite solar cells. *Sci. Adv.* **7**, eabj1363 (2021).

Acknowledgements

This work was supported by the National Research Foundation of Korea (NRF) grant funded by the Korea government (MSIP) (grant nos. RS-2023-00208467 to J.H.N. and RS-2025-02316700 to J.H.N.) and Korea Institute of Energy Technology Evaluation and Planning (KETEP) grant funded by the Ministry of Trade, Industry, and Energy (grant no. 20214000000680 to J.H.N.). This work was also supported by Technology Innovation Program of the Korea Evaluation Institute of Industrial Technology (KEIT) (20016588 to M.C.) funded by Ministry of Trade, Industry and Energy (MOTIE) and by Basic Science Research Program through the National Research Foundation of Korea (NRF) funded by the Ministry of Education (grant no. 2021R1A6A3A13046255 to S.L.), and by the Korea Research Institute of Chemical Technology (KRICT) (project no. KS2522-30 to T.J.S). The DFT calculations were performed using computational resources sponsored by the DOE Office of Energy Efficiency and Renewable Energy and located at NREL, and the resources of the National Energy Research Scientific Computing Center (NERSC), a DOE Office of Science User Facility located at Lawrence Berkeley National Laboratory, operated under contract no. DE-AC02-05CH11231 using NERSC award BES-ERCAP0032847 (to Y.Y.).

Author contributions

S.L. contributed to the conceptualization, fabrication and characterization for photovoltaic devices, stability test for photovoltaic devices, investigation, visualization and original draft. Y.-W.J. contributed to the conceptualization, synthetization and analysis of 2D perovskite; fabrication and characterization for photovoltaic devices; investigation; visualization; and original draft. J.H.N. contributed to the conceptualization, funding acquisition, project administration, supervision and original draft. M.C. contributed to the conceptualization and funding acquisition. H.C. contributed to the fabrication, characterization and stability test for photovoltaic devices. W.C. contributed to the fabrication and characterization for photovoltaic devices. H.H. and W.H. contributed to the fabrication and characterization for narrow-bandgap devices. O.J.O., D.H. Kim and D.H. Kang contributed to characterization for stability of perovskite film. J.L., J.D.-J., P.R.D. and J.S.Y. contributed to the characterization and interpretation of AFM and PiFM. T.J.S. and H.J.M. contributed to the characterization and interpretation of grazing-incidence wide-angle X-ray scattering. J.X. and Y.Y. contributed to the DFT calculations.

Competing interests

J.H.N., S.L., D.H. Kim, H.H., W.H., O.J.O. and Y.-W.J. are inventors on a Korean patent application related to the technology reported in this work (Korean patent application no. 10-2025-0098833). The other authors declare no competing interests.

Additional information

Extended data is available for this paper at https://doi.org/10.1038/s41560-026-02027-4.

Supplementary information The online version contains supplementary material available at https://doi.org/10.1038/s41560-026-02027-4.

Correspondence and requests for materials should be addressed to Jun Hong Noh.

Peer review information *Nature Energy* thanks Ruipeng Li and the other, anonymous, reviewer(s) for their contribution to the peer review of this work.

Reprints and permissions information is available at www.nature.com/reprints.

Publisher's note Springer Nature remains neutral with regard to jurisdictional claims in published maps and institutional affiliations.

[1]School of Civil, Environmental and Architectural Engineering, Korea University, Seoul, Republic of Korea. [2]Wright Center for Photovoltaics Innovation and Commercialization, Department of Physics and Astronomy, University of Toledo, Toledo, OH, USA. [3]Global Frontier Center for Multiscale Energy Systems, Seoul National University, Seoul, Republic of Korea. [4]Department of Mechanical and Aerospace Engineering, Seoul National University, Seoul, Republic of Korea. [5]Department of Chemical and Biomolecular Engineering, Rice University, Houston, TX, USA. [6]Australian Centre for Advanced Photovoltaics, School of Photovoltaic and Renewable Energy Engineering, University of New South Wales, Sydney, New South Wales, Australia. [7]Department of Materials Science and Engineering, Chonnam National University, Gwangju, Republic of Korea. [8]Graduate School of Semiconductor Materials and Devices Engineering, Ulsan National Institute of Science and Technology, Ulsan, Republic of Korea. [9]School of Computer Science and Electronic Engineering, Advanced Technology Institute, University of Surrey, Guildford, UK. [10]KU-KIST Graduate School of Converging Science and Technology, Korea University, Seoul, Republic of Korea. [11]Cardiff Catalysis Institute, School of Chemistry, Cardiff University, Cardiff, UK. [12]Department of Integrative Energy Engineering, Korea University, Seoul, Republic of Korea. [13]These authors contributed equally: Seungmin Lee, Yeoun-Woo Jang. ✉e-mail: junhnoh@korea.ac.kr

https://doi.org/10.1038/s41560-026-02027-4

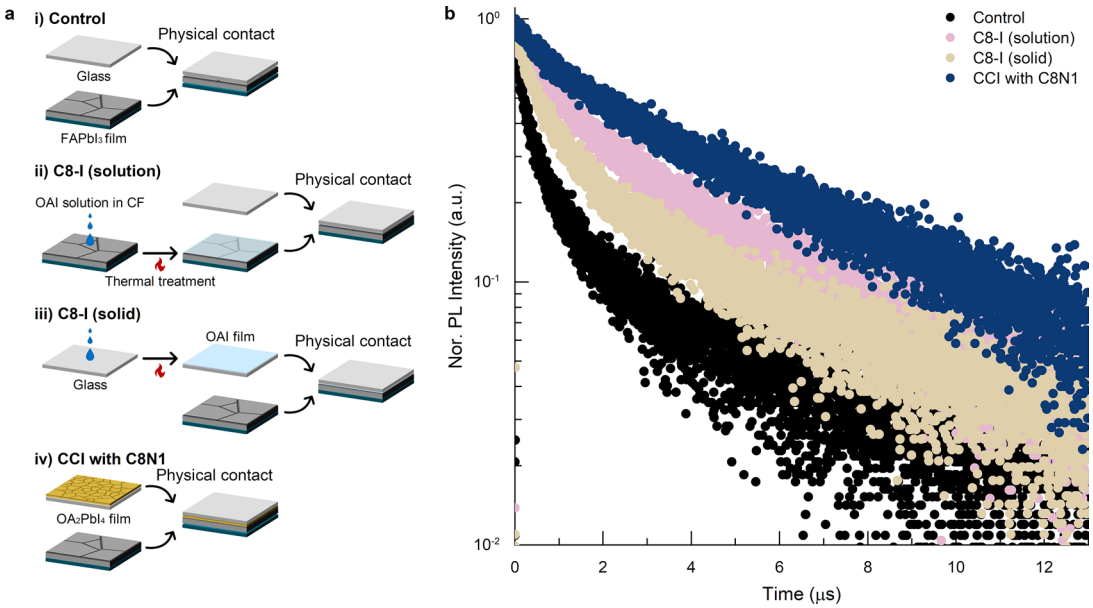

Extended Data Fig. 1 | PL decay behavior for different octylammonium spacer contact configurations. a, Schematic illustration of octylammonium (C8) spacer contact configurations for interface formation: i) control, ii) solution-processed octylammonium iodide (C8-I) treatment, iii) solid-state C8-I film, and iv) CCI formation using the framework-embedded C8 spacer configuration. No additional post-treatments were applied after physical contact. **b**, Comparison of PL decay for the same C8 spacer in different contact configurations.

https://doi.org/10.1038/s41560-026-02027-4

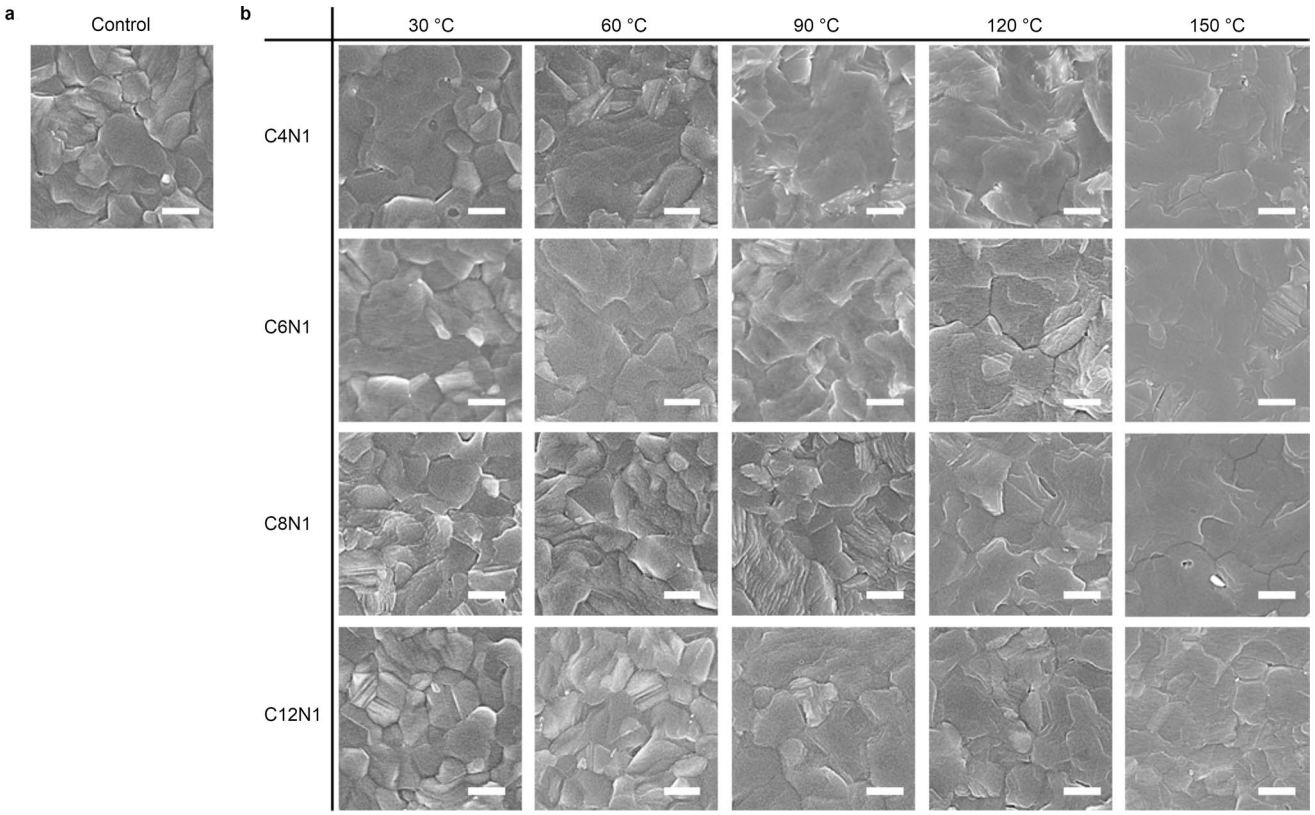

Extended Data Fig. 2 | Surface morphologies of 3D perovskite via CCI with varying spacer adsorption energies and processing temperatures. **a**, Top-view SEM image of the control 3D $FAPbI_3$ film. **b**, Surface morphologies of $FAPbI_3$ films after CCI treatment using various 2D perovskite films (C4N1, C6N1, C8N1, and C12N1) over a processing temperature range of 30 °C to 150 °C with 30 °C increments. The adsorption energy of the spacers increases in the order C4N1 < C6N1 < C8N1 < C12N1. Scale bars, 1 μm.

https://doi.org/10.1038/s41560-026-02027-4

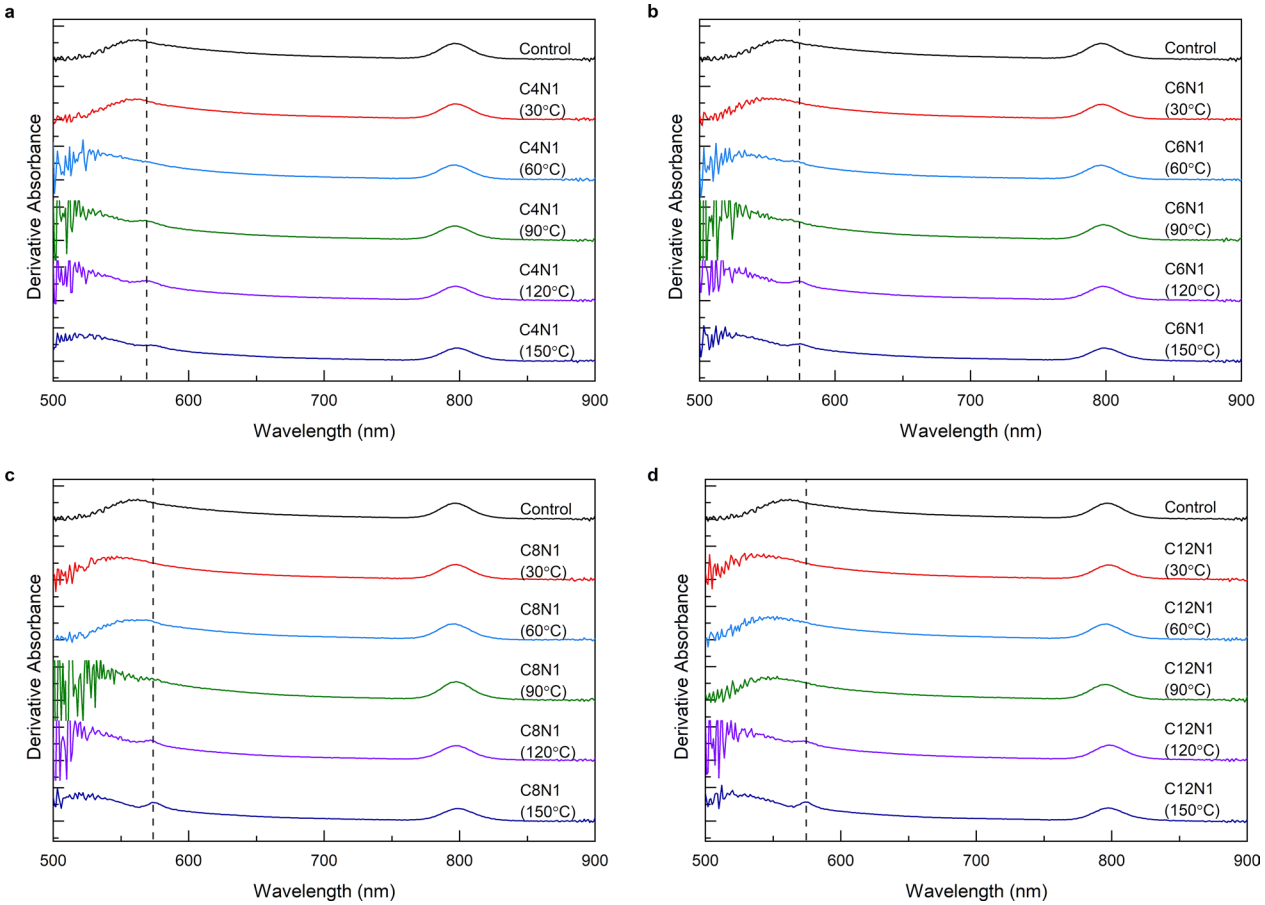

Extended Data Fig. 3 | Evolution of derivative absorbance spectra under CCI conditions. a–**d**, Derivative absorbance plots of $FAPbI_3$ films processed with (**a**) C4N1, (**b**) C6N1, (**c**) C8N1, and (**d**) C12N1 2D perovskites. The processing temperatures are indicated in the legends. Vertical dashed lines mark the absorption feature corresponding to the $n = 2$ quasi-2D perovskite phase. The adsorption energy of the spacers increases in the order C4N1 < C6N1 < C8N1 < C12N1.

https://doi.org/10.1038/s41560-026-02027-4

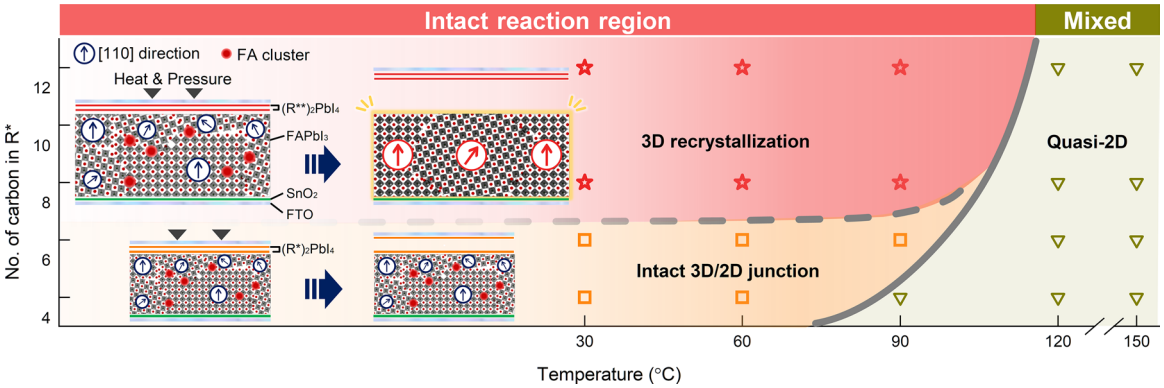

Extended Data Fig. 4 | Map of 3D perovskite outcomes under CCI as a function of spacer adsorption energy and processing temperature. The outcomes are classified into three regions: 3D recrystallization (red), intact 3D/2D junction formation (orange), and mixed quasi-2D phase formation (green). The insets schematically illustrate mechanisms within the intact reaction region: 3D recrystallization (top) and intact 3D/2D junction formation (bottom).

https://doi.org/10.1038/s41560-026-02027-4

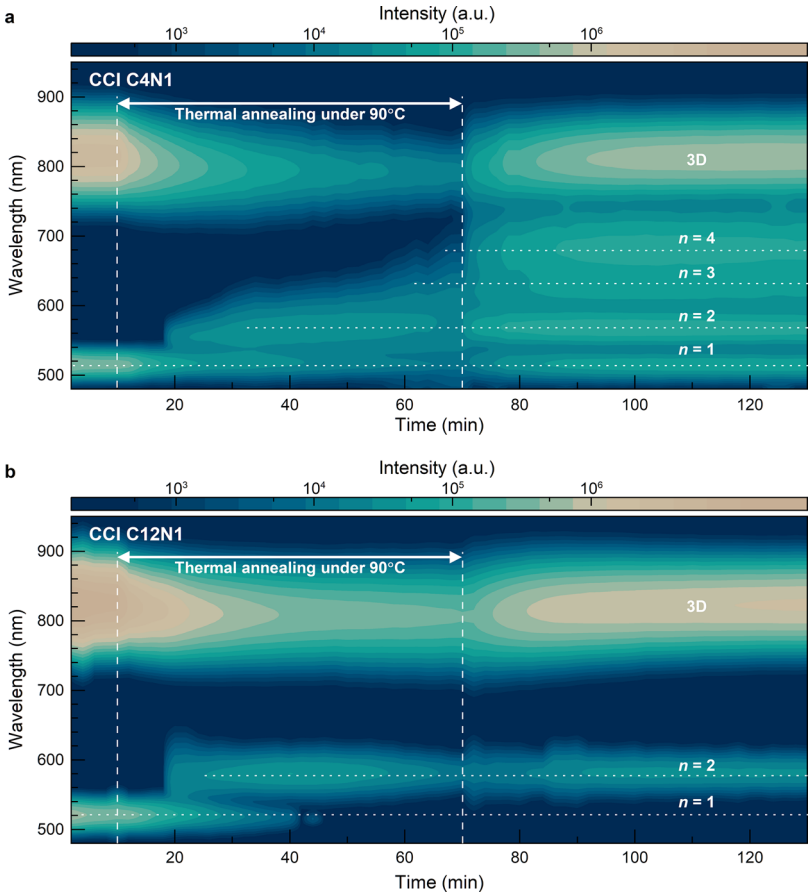

Extended Data Fig. 5 | In situ PL mapping under different CCI conditions. **a**, **b**, Contour maps of PL intensity evolution for (**a**) C4N1 and (**b**) C12N1 in contact with $FAPbI_3$. 3D and 2D perovskite films were placed in direct physical contact with each other. The excitation light was incident from the 2D perovskite side while PL spectra were recorded at equal time intervals. Annealing started 10 min after the measurement began, continued for 60 min, and was then stopped. To exclude thermal effects, the sample was subsequently cooled to room temperature for 1 h.

https://doi.org/10.1038/s41560-026-02027-4

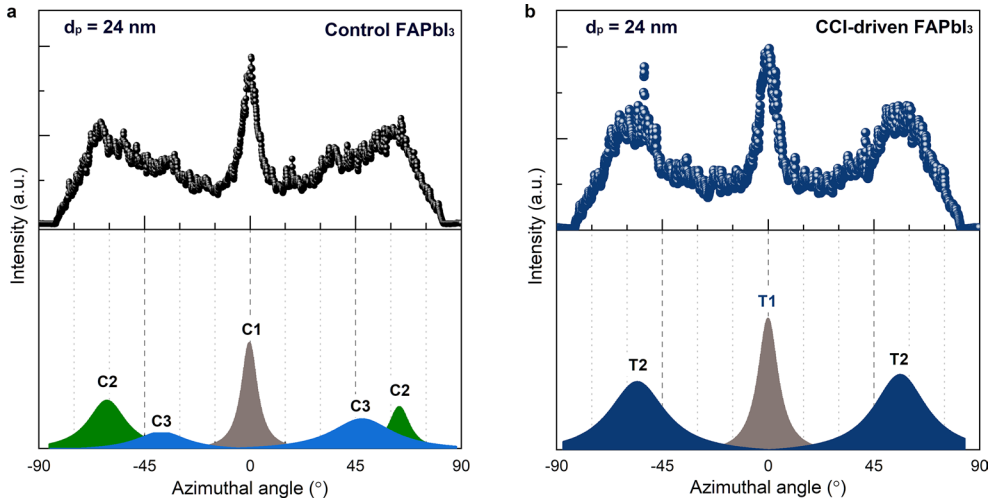

Extended Data Fig. 6 | Azimuthal orientation distributions for recrystallization via CCI with C8N1. a, **b**, Azimuthal intensity profiles of the $(110)_t$ plane ring of (**a**) control $FAPbI_3$ and (**b**) CCI-driven $FAPbI_3$ at an incident angle α_i of 0.117° (penetration depth d_p ~ 24 nm).

nature portfolio

Corresponding author(s): Jun Hong Noh

Solar Cells Reporting Summary

Nature Portfolio wishes to improve the reproducibility of the work that we publish. This form is intended for publication with all accepted papers reporting the characterization of photovoltaic devices and provides structure for consistency and transparency in reporting. Some list items might not apply to an individual manuscript, but all fields must be completed for clarity.

For further information on Nature Research policies, including our data availability policy, see Authors & Referees.

Experimental design

Please check the following details are reported in the manuscript, and provide a brief description or explanation where applicable.

1. Dimensions

Area of the tested solar cells	☒ Yes ☐ No	The tested solar cells were fabricated with geometric areas of 0.16 cm² and 1.1 cm². *Explain why this information is not reported/not relevant.*
Method used to determine the device area	☒ Yes ☐ No	The device areas were defined by the dimensions of the metal deposition masks. *Explain why this information is not reported/not relevant.*

2. Current-voltage characterization

Current density-voltage (J-V) plots in both forward and backward direction	☒ Yes ☐ No	J-V curves measured in both forward and reverse directions are presented in Fig. 5a and Supplementary Figs. 29, 30, 31, and 37. *Explain why this information is not reported/not relevant.*
Voltage scan conditions	☒ Yes ☐ No	Details are in the Method section (Characterization): 'The J-V curves were measured first in the reverse direction (1.2 V to -0.2 V), immediately followed by the forward direction (-0.2 V to 1.2 V), with a scan speed of 100 mV/s and a step voltage of 10 mV. *Explain why this information is not reported/not relevant.*
Test environment	☒ Yes ☐ No	The J-V measurements were conducted at room temperature in ambient air. *Explain why this information is not reported/not relevant.*
Protocol for preconditioning of the device before its characterization	☐ Yes ☒ No	No preconditioning protocol was applied prior to J-V characterization. *Explain why this information is not reported/not relevant.*
Stability of the J-V characteristic	☒ Yes ☐ No	The stabilized power output (SPO) tracked at the maximum power point is presented in Supplementary Fig. 28. *Explain why this information is not reported/not relevant.*

3. Hysteresis or any other unusual behaviour

Description of the unusual behaviour observed during the characterization	☒ Yes ☐ No	Negligible hysteresis was observed during the J-V sweeps. *Explain why this information is not reported/not relevant.*
Related experimental data	☒ Yes ☐ No	J-V curves measured in both forward and reverse directions are presented in Fig. 4a and Supplementary Figs. 29, 30, 31, and 37. *Explain why this information is not reported/not relevant.*

4. Efficiency

External quantum efficiency (EQE) or incident photons to current efficiency (IPCE)	☒ Yes ☐ No	EQE spectra are presented in Figs. 5b and Supplementary Fig. 39. *Explain why this information is not reported/not relevant.*
A comparison between the integrated response under the standard reference spectrum and the response measure under the simulator	☒ Yes ☐ No	The integrated Jsc values calculated from the EQE spectra are in good agreement with the Jsc obtained from J-V measurements. *Explain why this information is not reported/not relevant.*

For tandem solar cells, the bias illumination and bias voltage used for each subcell

☐ Yes
☒ No

Provide a description of the measurement conditions.

Not applicable to this work.

5. Calibration

Light source and reference cell or sensor used for the characterization

☒ Yes
☐ No

As detailed in the Characterization section, the devices were measured using a solar simulator (Newport, 94043A) coupled with a source meter (Keithley 2400).

Explain why this information is not reported/not relevant.

Confirmation that the reference cell was calibrated and certified

☒ Yes
☐ No

As detailed in the Characterization section, the light intensity was adjusted using certified reference cells (Newport) equipped with Quartz and KG3 filters.

Explain why this information is not reported/not relevant.

Calculation of spectral mismatch between the reference cell and the devices under test

☐ Yes
☒ No

Provide a value of the spectral mismatch and/or a description of how it has been taken into account in the measurements.

Although the spectral mismatch factor was not explicitly calculated, the calibration was tailored to the varying bandgaps of the devices by selectively using Quartz and KG3-filtered reference cells to match the spectral response.

6. Mask/aperture

Size of the mask/aperture used during testing

☒ Yes
☐ No

A circular aperture of 0.096 cm^2 was used for small-area devices, while a 1.00 cm^2 mask was employed for large-area devices. Both areas were verified via microscopy, with the 0.096 cm^2 aperture independently confirmed during the certification process at the Solar Energy Research Institute of Singapore.

Explain why this information is not reported/not relevant.

Variation of the measured short-circuit current density with the mask/aperture area

☐ Yes
☒ No

Report the difference in the short-circuit current density values measured with the mask and aperture area.

The variation in Jsc with respect to the aperture area was negligible.

7. Performance certification

Identity of the independent certification laboratory that confirmed the photovoltaic performance

☒ Yes
☐ No

The photovoltaic performance was independently confirmed by the Solar Energy Research Institute of Singapore.

Explain why this information is not reported/not relevant.

A copy of any certificate(s)

☒ Yes
☐ No

Copies of the certification reports are presented in Supplementary Fig. 29.

Explain why this information is not reported/not relevant.

8. Statistics

Number of solar cells tested

☒ Yes
☐ No

Eight devices were tested for each experimental condition.

Explain why this information is not reported/not relevant.

Statistical analysis of the device performance

☒ Yes
☐ No

Statistical analysis results are presented in Supplementary Fig. 32.

Explain why this information is not reported/not relevant.

9. Long-term stability analysis

Type of analysis, bias conditions and environmental conditions

☒ Yes
☐ No

Operational stability under maximum power point tracking and various thermal stress conditions is presented in Figs. 5c and 5d. Additionally, the phase stability of the perovskite material is demonstrated in Figs. 4g and 4h.

Explain why this information is not reported/not relevant.